

# Determination of the Proton's Weak Charge and its Constraints on the Standard Model

Roger D. Carlini,<sup>1</sup> W.T.H. van Oers<sup>2</sup>, Mark L. Pitt,<sup>3</sup> and G.R. Smith<sup>4</sup>

<sup>1</sup>Thomas Jefferson National Accelerator Facility, Newport News, VA, USA, 23606; email: carlini@jlab.org

<sup>2</sup>TRIUMF, Vancouver, BC, Canada, V6T2A3

<sup>3</sup>Virginia Polytechnic Institute & State University, Blacksburg, VA 24061 USA

<sup>4</sup>Thomas Jefferson National Accelerator Facility, Newport News, VA, USA, 23606

Annual Review of Nuclear and Particle Science 2019. 69:1–23

[https://doi.org/10.1146/\(\(please add article doi\)\)](https://doi.org/10.1146/((please add article doi)))

Copyright © 2019 by Annual Reviews.  
All rights reserved

## Keywords

parity-violating electron scattering, asymmetry, weak charge of the proton, vector quark couplings, running of the weak mixing angle, physics beyond the standard model

## Abstract

This article discusses some of the history of parity-violation experiments that culminated in the  $Q_{\text{weak}}$  experiment, which provided the first determination of the proton's weak charge  $Q_W^p$ . The guiding principles necessary to the success of that experiment are outlined, followed by a brief description of the  $Q_{\text{weak}}$  experiment. Several consistent methods used to determine  $Q_W^p$  from the asymmetry measured in the  $Q_{\text{weak}}$  experiment are explained in detail. The weak-mixing angle  $\sin^2 \theta_w$  determined from  $Q_W^p$  is compared to results from other experiments. A description of the procedure for using the  $Q_W^p$  result on the proton to set TeV-scale limits for new parity-violating semi-leptonic physics beyond the standard model (BSM) is presented. By also considering atomic parity-violation results on cesium, it is shown how this result can be generalized to set limits on BSM physics which couples to any combination of valence-quark flavors. Finally, the discovery space available to future weak charge measurements is explored.

## Contents

1. Introduction .....	2
1.1. Milestones in Accelerator-Based Parity-Violation Measurements .....	3
1.2. Isolating the Weak Charge of the Proton via a Parity-Violation Measurement.....	3
2. The Experiment .....	4
2.1. Guiding Design Principles .....	5
2.2. Technical Implementation.....	6
2.3. Determination of $A_{ep}$ .....	7
3. Extraction of the Weak Charge & Vector Quark Couplings.....	9
3.1. The Global Fit of the PVES Database .....	10
3.2. Determining $Q_W^p$ from the $Q_{\text{weak}}$ Datum & Calculated Form Factors .....	12
3.3. $Q_W^p$ from the $Q_{\text{weak}}$ Datum, PVES Database & Calculated Form Factors.....	13
4. The Running of $\sin^2 \theta_W$ .....	14
5. The Search for Physics Beyond the Standard Model.....	16
5.1. Constraints Provided by Weak Charge Experiments .....	16
5.2. Flavor-independent Constraints .....	18
5.3. Constraints on Specific BSM Extensions .....	18
6. Future Prospects .....	19
6.1. Experimental Challenges .....	19
6.2. Interpretability Challenges .....	20
7. Summary .....	21

## 1. Introduction

The Standard Model (SM) is the theory that unifies the strong, electromagnetic and weak interactions. To date it appears to be in excellent agreement with virtually all applicable experimental observables. With the observation of the Higgs boson at the LHC, the existence of the last particle explicitly predicted within the SM has now been confirmed (1, 2). However, the SM is known to be incomplete and likely the low-energy approximation of what needs to be a more extensive theoretical framework that accommodates a larger set of physical phenomena. Some of the known limitations of the SM include: The inability to predict some key features of particles within the model’s framework, the lack of any straightforward means to include gravity, the inability to account for the existence of dark energy (a candidate for the explanation of the observed accelerated expansion of the universe) or dark matter that is believed to account for most of the mass of the universe, and issues with the hierarchies of scale related to the Higgs boson. These various limitations, along with the dearth of new particles observed in the post-Higgs era, have left the theoretical door open for physics beyond the Standard Model (BSM) to be observable at the TeV scale. The TeV scale can be selectively probed by precision tests of fundamental symmetries in parity-violation (PV), electric dipole moment measurements,  $g-2$  (anomalous magnetic moment of the muon) experiments, neutrino scattering and other accelerator-based experiments (see (3, 4)). These types of measurements provide a means of reaching mass scales not directly accessible at existing high-energy colliders.

### 1.1. Milestones in Accelerator-Based Parity-Violation Measurements

It has long been understood that the contribution of the weak force in particle interactions can be isolated and studied by conducting PV measurements. This is possible because within the SM only those interactions mitigated by the weak force change sign with the helicity of the particles involved. This section tries to summarize a few key milestones and does not attempt to be comprehensive or do justice to all the significant technical and scientific accomplishments of the generations of scientists working in this field.

The era of accelerator-based PV measurements had its origin at Los Alamos with the first non-zero result in 1974 of hadronic PV in proton-proton scattering at 15 MeV (5), by Nagle, McKibben, Potter and colleagues. The measurement was performed at a tandem with a Lamb-shift polarized-ion source employing the initial use of rapid spin-reversal (1 kHz) of a 200 nA longitudinally-polarized proton beam and phase-locking analog-signal-processing electronics to measure the normalized asymmetry  $A_z$  in the total cross-section for the two spin-states. This effort helped motivate a generation of higher-energy polarized-proton measurements at Los Alamos/LAMPF, TRIUMF, PSI and other laboratories. These PV programs were for the most part able to achieve their scientific goals while pioneering and expanding the experimental methodology, polarized-source technology, handling of beam-related systematic uncertainties and achieving a relatively high degree of precision. They unambiguously observed the weak interaction in complex systems. However, because of their limited kinematics and theoretical interpretability they were not able to search for BSM physics.

The next major leap forward came by applying key methodologies (primarily rapid helicity-reversal, phase-locking signal detection and precise beam-property control) to electron accelerators at MIT/BATES, Mainz and SLAC. This new generation of PV measurements could now benefit from the structureless nature of the electron probe that for the first time made possible the interpretation of results in terms of quantities that are precisely predicted by the SM, even with measurement precision significantly less than those already achieved with proton probes. The seminal electron-accelerator PV measurement was the SLAC E122 experiment of Prescott, Hughes and colleagues (6), which clearly observed the presence of PV in the neutral weak current and was critical to establishing universal acceptance of the electroweak Standard Model.

However, the most recent generation of completed experiments would for the first time probe for evidence of possible BSM physics. These experiments achieved a precision of a few ppb in the measurement of the scattering asymmetry. The two major efforts were SLAC-E158 (7) and  $Q_{\text{weak}}$  at JLab (8). Although these measurements were both technically successful, neither found a significant discrepancy between measurement and the corresponding SM prediction.

### 1.2. Isolating the Weak Charge of the Proton via a Parity-Violation Measurement

The metrics for a PV measurement are not simply precision and accuracy, but that the observable(s) be clearly interpretable with respect to what is predicted by theory. In the case of the measurement of  $Q_W^p$  that theory is the SM. Any significant deviation between the measured and predicted value of  $Q_W^p$  would be an indication of BSM physics, whereas agreement would place new and significant constraints on possible SM extensions. The  $Q_{\text{weak}}$  experiment's determination of  $Q_W^p$  was relatively clean with respect to theoretical

interpretability, as the experiment's primary analysis-technique relied on experimental data, not theoretical calculations, to remove any remnant hadronic-backgrounds after already heavy suppression by the kinematics selected for the measurement (8). In conjunction with existing higher  $Q^2$  parity-violating electron-scattering (PVES) data, the extraction of  $Q_W^p$  and the weak neutral-current vector-coupling constants  $C_{1q}$  is straightforward, allowing the evaluation of possible scenarios of physics BSM.

The experimentally-observed quantity is the asymmetry  $A_{ep}$  in the elastic-scattering cross-section of longitudinally-polarized electrons (with helicity  $\pm 1$ ) from an unpolarized-proton target:

$$A_{ep} = \frac{\sigma_+ - \sigma_-}{\sigma_+ + \sigma_-}, \quad 1.$$

When expressed in terms of Sachs electromagnetic (EM) form factors  $G_E^\gamma, G_M^\gamma$ , weak neutral form factors  $G_E^Z, G_M^Z$  and the neutral weak axial form factor  $G_A$ , this asymmetry has the form:

$$A_{ep} = \left[ \frac{-G_F Q^2}{4\pi\alpha\sqrt{2}} \right] \left[ \frac{\varepsilon G_E^\gamma G_E^Z + \tau G_M^\gamma G_M^Z - (1 - 4 \sin^2 \theta_W) \varepsilon' G_M^\gamma G_A^Z}{\varepsilon (G_E^\gamma)^2 + \tau (G_M^\gamma)^2} \right] \quad 2.$$

where

$$\varepsilon = \frac{1}{1 + 2(1 + \tau) \tan^2 \frac{\theta}{2}}, \quad \varepsilon' = \sqrt{\tau(1 + \tau)(1 - \varepsilon^2)} \quad 3.$$

are kinematical quantities,  $Q^2$  is the four-momentum transfer,  $\tau = Q^2/4M^2$  where  $M$  is the proton mass,  $G_F$  is the Fermi coupling constant,  $\alpha$  is the fine structure constant and  $\theta$  is the laboratory electron scattering-angle. For forward-angle scattering where  $\theta \rightarrow 0$ ,  $\varepsilon \rightarrow 1$ , and  $\tau \ll 1$ , the asymmetry can then be written as:

$$A_{ep} = A_0 [Q_W^p + Q^2 B(Q^2, \theta)], \quad \text{where } A_0 = \left[ \frac{-G_F Q^2}{4\pi\alpha\sqrt{2}} \right]. \quad 4.$$

The first term, proportional to  $Q^2$ , corresponds to a point-like proton. The second term  $B(Q^2, \theta)$ , proportional to  $Q^4$ , is the leading term in the nucleon structure defined in terms of neutron and proton EM and weak form factors. While the nucleon-structure contributions in  $B(Q^2, \theta)$  can be suppressed by employing lower momentum-transfer  $Q^2$ , this also has the consequence of reducing the measurement's asymmetry, making (for example) the control of helicity-correlated beam properties relatively more important. Therefore, these trade-offs were investigated as part of the optimization of the experiment. Fortunately, the numerical value of  $B(Q^2, \theta)$  can be determined accurately by extrapolation from existing PVES data at higher  $Q^2$ . After folding in the available choices for the primary beam-energy, scattering kinematics and practical topologies for the apparatus/detector, the optimum  $Q^2$  to perform the  $Q_W^p$  measurement was determined to be  $0.0248 \text{ (GeV/c)}^2$ , a beam energy of  $1.16 \text{ GeV}$  and a central electron scattering-angle  $\theta = 7.9^\circ$  in the laboratory frame.

## 2. The Experiment

The  $Q_{\text{weak}}$  experiment was an integrating measurement (rather than counting events one at a time), meaning except for  $Q^2$  acceptance studies at very low beam-currents, the ability to apply traditional data-cuts and corrections post data-collection was somewhat limited. Therefore, the data collected had to be of very high quality upfront. This is the price all

integrating measurements pay in order to achieve the necessary ultra-high statistical precision. Performing a PV experiment with enough accuracy to be a meaningful test for BSM physics requires measuring the scattering asymmetry at appropriate kinematics (as discussed above), which means balancing the requirement to obtain good counting-statistics with the requirement to maintain sufficient control of the instrumental and background systematics. These considerations impose significant design constraints on beam properties (energy, position, angle, size, current, and polarization), experimental acceptance, spectrometer design, and all the experimental sub-systems that measure systematic effects.

## 2.1. Guiding Design Principles

The measurement was performed by comparing the scattering rate for the two opposite longitudinal helicity-states of the electron beam. Ideally, no property of the apparatus or beam is changed when the longitudinal helicity of the electron beam is reversed, as such changes can give rise to false asymmetries that contaminate the measurement of the physics asymmetry. In practice, such changes always exist to some degree. So in addition to simply measuring them in order to correct any residual non-zero false asymmetries, experiments must be designed to be as insensitive as possible to these effects. Identifying these contributions and suppressing them is dealt with in part by having multiple helicity-reversals on a variety of timescales. The minimization of such false-asymmetry effects is also aided by passive measures such as complete isolation of the helicity signal from the rest of the apparatus and symmetric-apparatus design, as well as active measures such as feedback systems to minimize the amount by which beam properties can change under helicity-reversal. Finally, any remaining non-zero sources of false asymmetry need specialized instrumentation designed to measure and correct for them to the precision required by the scientific goals of the measurement.

The  $Q_{\text{weak}}$  experiment was optimized in a number of other ways as well. The eight-sector toroidal magnetic-spectrometer concept was selected to increase acceptance to approximately 49% of  $2\pi$  in  $\phi$ , separate elastic from in-elastic events and to provide an intrinsic suppression of the net effect of scattering asymmetries from the small residual transverse-polarization (several percent) in the otherwise longitudinally-polarized electron beam. The beam energy (1.16 GeV) provided by the CEBAF accelerator permitted a topology of the magnet-detector layout which among other attributes allowed heavy line-of-sight shielding between the detectors and the target/beamline, including a shutter system to selectively block an octant of the collimator system when conducting detector background-studies. The following are a number of additional considerations that guided the detailed design of the experiment:

- Maximizing the figure-of-merit (FOM) to achieve ppb-level precision. The FOM is the inverse of the fractional statistical error on  $Q_W^p$  squared. Although a useful metric, it's not a measure of the difficulty of the experiment, which would have to consider systematic errors as well. For a fixed running time, the FOM can be expressed as

$$\text{FOM} = \frac{A_{ep}^2 P^2 R}{\left(1 + \frac{Q_0^2 B(Q_0^2, \theta_0)}{Q_W^p}\right)^2}, \quad 5.$$

where  $A_{ep}$  is the physics asymmetry,  $P$  is the beam polarization,  $R$  is the total elastic scattering rate, and  $Q_0^2$  and  $\theta_0$  are the central kinematics values. The term

in the denominator reflects the fact that it is only the first term in the asymmetry Equation 4 that is sensitive to  $Q_W^p$ , so the figure-of-merit is increased by reducing the contribution of the second term that represents the hadronic structure.

- The instrumentation of key signals (the primary detector and beam-current-monitor systems) with ultra-low-noise analog and digital electronics so the experimental apparatus operates as close as possible to "counting statistics" near the helicity-reversal frequency. This is essential to minimize the running time necessary to achieve the desired precision. Similar care is necessary in the cryogenic target design to minimize the "noise" contribution due to density variations (boiling).
- Incorporation of "NULL asymmetry" measurements to quantify (or ideally verify) the absence of false asymmetries.
- Redundancy: Allows important cross-check capability and resiliency during data analysis. This includes multiple methods/devices for measurement of beam polarization, beam current, beam position, helicity-correlated beam asymmetries (HCBAs), backgrounds, helicity reversal, etc.
- Multiple run periods: to improve and compare results under different conditions.
- Always remember that unprecedented precision brings inevitable surprises. Therefore, incorporate ancillary detectors and capabilities to handle unexpected backgrounds.
- Blind the analysis to suppress experimenter bias.
- Use cutting-edge technology but avoid non-essential use of unproven technology.

## 2.2. Technical Implementation

The essential sub-systems of the  $Q_{\text{weak}}$  experiment are described in detail in (9) and shown schematically in **Figure 1**. The incorporation of instrumental redundancy cannot be emphasized enough for these types of precision measurements. The measurement was performed with an electron beam of  $180 \mu\text{A}$  at  $1.16 \text{ GeV}$  with an average polarization of 89%, which was incident on a  $0.344 \text{ m}$ -long  $20.00^\circ \text{ K}$  liquid-hydrogen target contained in an aluminum cell with thin entrance and exit windows. A set of three precisely-made lead collimators defined the scattering-angle acceptance to the range  $5.8^\circ < \theta < 11.6^\circ$  with an azimuthal angle coverage of 49% of  $2\pi$ . The scattered particles entered the eight open-sections of a toroidal resistive-magnet located between the target and the detectors. This "spectrometer" separated the elastically-scattered electrons from backgrounds consisting of inelastically-scattered particles, Møller electrons and neutral particles. The toroidal spectrometer was azimuthally symmetric around the incident-beam axis in order to negate the first order effects of helicity-correlated beam-parameter imperfections and residual transverse beam-polarizations on the measured asymmetries.

The high rates encountered ( $\sim 0.9 \text{ GHz}$  per detector) required a current-mode readout, in which the photomultiplier-tube (PMT) anode current was converted to a voltage that was integrated and digitized every  $1/960$  of a second. PMTs (with swappable low- and high-gain bases) were employed instead of vacuum photodiodes in order to allow periodic pulse-counting experiments to be performed for acceptance-weighted energy-distribution determinations at incident electron-beam currents of  $0.1 \text{ nA}$  to  $200 \text{ nA}$  with drift chambers placed before and after the toroidal magnetic spectrometer. An ancillary symmetric-array of four smaller detectors, so-called upstream luminosity-monitors, placed on the upstream face of the defining middle-collimator allowed monitoring residual backgrounds from the tungsten/copper beam-collimator which shielded the downstream region from small-angle

scattered particles. Residual diffuse-background was monitored by background detectors in the main-detector shield-bunker.

The GaAs polarized source of electrons and the injector to CEBAF delivered  $180 \mu\text{A}$  of longitudinally polarized electrons to the recirculating linac, but also delivered intensities of less than 1 nA for control, background and acceptance measurements. The helicity of the polarized-electron beam was reversed at a rate of 960 Hz in a pseudo-random sequence of helicity quartets of  $(+ - - +)$  or  $(- + + -)$ . This rapid spin-reversal also suppressed the noise component due to fluctuations in the cryogenic liquid-hydrogen target density as well as variations in the parameters of the accelerated electron-beam. A photographic analogy would be a frame-rate high enough that the scene changes only a minuscule amount from image to image. In addition to the rapid spin-reversal, two independent methods on a slower time-scale of the electron-beam helicity were used to observe/cancel possible false asymmetries. The first one was introduced every eight hours by changing the helicity of the laser beam impinging on the GaAs by insertion of a half-wave plate in its path. The second one was introduced monthly by changing the helicity of the electron beam in the injector section with a double-Wien spin rotator. In addition, by calculating an out-of-phase combination of the various slow helicity-reversals it was possible to construct a NULL version of the scattering asymmetry which should be zero. It was measured and found to indeed be consistent with zero, implying that all consequential helicity-correlated systematic effects had been accounted for.

Helicity-correlated changes in the accelerated-beam parameters (intensity, position, angle, size, and energy) may lead to false contributions to the measured asymmetries. The effects of helicity-correlated changes in the beam parameters were suppressed by careful tuning of the helicity-defining optics and by active-feedback systems in the polarized-injector laser system and beam transport-line. A series of beam monitors upstream of the experimental apparatus provided continuous, non-invasive measurement of the beam intensity, position, angle, and energy. The response of the experimental apparatus to fluctuations in the beam parameters was measured in a periodic manner through a beam-modulation system that introduced controlled variations in the beam position, angle, and size using various magnets along the beam-transport line; similarly in the beam energy using a radio-frequency accelerating cavity. It was also possible to measure these responses using the random natural beam-motion, but without being able to separate the effects on beam parameters one at a time.

### 2.3. Determination of $A_{ep}$

Here we summarize the highlights of how the parity-violating elastic electron-proton asymmetry was obtained in the  $Q_{\text{weak}}$  experiment. Full details of the data analysis that led to that result are presented in (8).

In the  $Q_{\text{weak}}$  experiment, the basic measurement consisted of averaging the 16 integrated Čerenkov light signals from both PMTs on each of the eight main detectors, and digitizing these values for each helicity state (every  $\sim\text{ms}$ ). These values were normalized to the beam charge. The charge-normalized yields ( $Y_{\pm}$ ) from each helicity quartet formed the raw asymmetry:

$$A_{\text{raw}} = \frac{Y_+ - Y_-}{Y_+ + Y_-}. \quad 6.$$

About 1.3 billion such "quartets" were collected over the course of one calendar year of

running. The resulting average raw-asymmetry was corrected for a variety of effects that could cause false asymmetries:

$$A_{\text{msr}} = A_{\text{raw}} + A_T + A_L + A_{\text{BCM}} + A_{\text{BB}} + A_{\text{beam}} + A_{\text{bias}}. \quad 7.$$

Here corrections were made for transverse asymmetry ( $A_T$ ), detector-signal linearity ( $A_L$ ), beam-current monitors ( $A_{\text{BCM}}$ ), beamline-background asymmetry ( $A_{\text{BB}}$ ), helicity-correlated beam properties ( $A_{\text{beam}}$ ), and a re-scattering bias ( $A_{\text{bias}}$ ). The measured asymmetry  $A_{\text{msr}}$  was then corrected for additional effects to obtain the fully-corrected parity-violating elastic electron-proton asymmetry:

$$A_{ep} = R_{\text{tot}} \frac{A_{\text{msr}}/P - \sum_{i=1,3,4} f_i A_i}{1 - \sum_{i=1}^4 f_i}. \quad 8.$$

The corrections here are for incomplete beam-polarization ( $P$ ), finite acceptance and (electromagnetic) radiative corrections ( $R_{\text{tot}}$ ), and the signal dilutions ( $f_i$ ) and asymmetries ( $A_i$ ) associated with background processes. In **Table 2**, we summarize the main contributions to the uncertainty for  $A_{ep}$ . The statistical uncertainty dominated, with the main contributions to the systematic uncertainty coming from:

- Rescattering bias ( $A_{\text{bias}}$ ): Rescattering of the partially transversely-polarized scattered electrons in the lead preradiators of the main detector led to a helicity-dependent light profile along the quartz bars. This effect was not anticipated prior to the experiment, but the symmetric readout of the quartz bars with PMTs at each end and the excellent uniformity of the quartz bars ultimately made this a small effect (10).
- Beam-current-monitor correction ( $A_{\text{BCM}}$ ): The beam current was measured non-invasively with radio-frequency resonant cavities. The observed variation in several such cavities determined the systematic uncertainty.
- Target-windows correction ( $A_{b1}$ ): The thin (0.1 mm) entrance and exit windows of the hydrogen target-cell were made of aluminum 7075 alloy which contributed  $\sim 2.5\%$  to the signal. The asymmetry in scattering from this alloy was measured in dedicated runs with a thick solid-target made of the same material as the windows (11, 12, 13).
- Beamline-background asymmetry correction ( $A_{\text{BB}}$ ): A small contribution ( $\sim 0.19\%$  of the detector signal) came from scattered electrons interacting in the beamline and tungsten/copper beam-collimator. These events carried a large asymmetry. This effect was not anticipated prior to the experiment, but auxiliary detectors had been installed for such unanticipated false-asymmetries. They were able to characterize this asymmetry so that a correction could be made (14).
- Helicity-correlated beam-property correction ( $A_{\text{beam}}$ ): Residual non-vanishing helicity-correlations in the properties of the electron beam were measured and corrected for through detector responses determined using a beam-modulation system (15).
- Kinematics ( $R_{Q^2}$ ): The central  $Q^2$  for the experiment was determined from simulation (16), and benchmarked with measurements from a tracking system that operated in counting mode during special low beam-current runs.
- Longitudinal beam polarization ( $P$ ): Beam polarization was measured redundantly with a Compton polarimeter (18) that operated continuously during the run and a Møller polarimeter (17) that operated invasively at low ( $\sim 2\mu\text{A}$ ) beam-currents.

The final result for the fully-corrected asymmetry was  $A_{ep} = -226.5 \pm 7.3(\text{stat}) \pm 5.8(\text{syst})$  ppb. This was determined at an acceptance-averaged  $Q^2$ , scattering angle and incident electron-energy of  $\langle Q^2 \rangle = 0.0248$  (GeV/c)<sup>2</sup>,  $\langle \theta \rangle = 7.90^\circ$  and  $\langle E_0 \rangle = 1.149$  GeV, respectively.

### 3. Extraction of the Weak Charge & Vector Quark Couplings

Several methods have been explored to extract the weak charge of the proton  $Q_W^p$  from measurements of the parity-violating asymmetries in  $\bar{e}p$ ,  $\bar{e}d$ , and  $\bar{e}^4\text{He}$  elastic scattering. These measurements define the parity-violating electron-scattering (PVES) database, and are loosely grouped into experiments performed by the SAMPLE (19, 20), PVA4 (21, 22, 23, 24), G0 (25, 26), HAPPEX (27, 29, 28, 30, 31) and  $Q_{\text{weak}}$  (32, 8) collaborations. The primary method used to extract  $Q_W^p$  was described in (32), where the commissioning result of the  $Q_{\text{weak}}$  experiment was presented, constituting about 4% of the total data acquired. The final results of the complete  $Q_{\text{weak}}$  experiment (8) were published in 2018, and constitute the best information currently available on the proton's weak charge. That result also provided the most precise measure of  $\sin^2 \theta_W$  below the Z-pole as discussed in Section 4, and the best mass-limit associated with parity-violating (PV) semi-leptonic (SL) physics beyond the standard model (BSM), as discussed in Section 5. Results from several methods used to determine  $Q_W^p$  from the  $Q_{\text{weak}}$  experiment's asymmetry with and without the other asymmetries in the PVES database were also presented in (8). We detail those methods here along with the results that came from them, and then introduce a new and simpler method which is consistent with the results obtained from the other methods.

In the "primary" method described in (32, 8), the weak vector quark couplings  $C_{1u}$  and  $C_{1d}$ , the strength of the strange form factors  $G_{E,M}^s$ , and the isovector axial form factor  $G_A^{Z(T=1)}$  were varied in a fit of the PVES asymmetries up to  $Q^2 = 0.63$  GeV<sup>2</sup>. The proton's weak charge was obtained by extrapolating that fit to  $Q^2 = 0$ . This method is preferred because it's data-driven: the measured asymmetries in the PVES database were used to pin down the hadronic-structure contributions ( $G_{E,M}^s$  and  $G_A^{Z(T=1)}$ ) in order to determine  $Q_W^p$ . In this as well as the other methods described below to determine  $Q_W^p$  from PVES asymmetries, the dominant contribution to the hadronic structure comes from the relatively well-known EM form factors  $G_{E,M}$  taken from (33).

Alternatively, as discussed in (8) the hadronic structure contributions can be *calculated* instead of determined from data in the fit described above. This is necessary when using the  $Q_{\text{weak}}$  datum alone to determine  $Q_W^p$ . At the low  $Q^2$  of the  $Q_{\text{weak}}$  experiment, the contributions from  $G_{E,M}^s$  and  $G_A^Z$  to  $Q_W^p$  are small ( $\sim 2\%$ ). But it's also interesting and informative to use this technique (calculating  $G_{E,M}^s$  and  $G_A^Z$ ) in a straight-line fit to each  $Q_W^p$  determined at the respective  $Q^2$  of each asymmetry measured in the PVES database. In that case the best fit is (linear and) nearly constant, since to the extent we know  $G_{E,M}^s$  and  $G_Z$ ,  $Q_W^p$  should be the same number independent of  $Q^2$ . This new method also helps expose a slight tension between the fit and calculated strange form factors at higher  $Q^2$ .

In this section, we explain how each of these methods is implemented and examine the consistency of the results obtained for  $Q_W^p$ . These results are compared with one another and with the SM in Figure 2.

### 3.1. The Global Fit of the PVES Database

The starting point for relating the PV asymmetry measured in the  $Q_{\text{weak}}$  experiment to the weak charge of the proton  $Q_W^p$  is the tree-level (one-boson exchange) formula in Equation 2. In that equation, the proton's weak neutral form factor  $G_{E,M}^{pZ}$  can be expressed in terms of proton, neutron, and strange quark EM form factors by making use of isospin symmetry:

$$G_{E,M}^{p/n,i} = e^{i,u} G_{E,M}^{u/d} + e^{i,d} (G_{E,M}^{d/u} + G_{E,M}^s). \quad 9.$$

Then with ( $i = \gamma, Z$ ), and inserting the ordinary EM ( $\gamma$ ) charges for the ( $u, d$ , and  $s$ ) quarks: ( $e^\gamma = +2/3 (u), -1/3 (d, s)$ ), as well as the weak quark-charges: ( $e^Z = 1 - 8/3 \sin^2 \theta_W (u), -1 + 4/3 \sin^2 \theta_W (d, s)$ ), it follows straightforwardly that

$$G_{E,M}^{pZ} = (1 - 4 \sin^2 \theta_W) G_{E,M}^{p\gamma} - G_{E,M}^{n\gamma} - G_{E,M}^{s\gamma} = Q_W^p G_{E,M}^{p\gamma} - G_{E,M}^{n\gamma} - G_{E,M}^{s\gamma}. \quad 10.$$

Inserting Equation 10 into 2, we can write the asymmetry in terms of the proton's weak charge  $Q_W^p$  and its extended structure expressed in terms of EM ( $A_{EM}$ ), strange quark ( $A_s$ ), and axial ( $A_{ax}$ ) components as

$$A/A_0 = Q_W^p - (A_{EM} + A_s + A_{ax}), \quad \text{where} \quad 11.$$

$$A_{EM} = A_E + A_M = \left( \epsilon (G_E^p G_E^n)^2 + \tau (G_M^p G_M^n)^2 \right) / D, \quad 12.$$

$$A_s = A_E^s + A_M^s = \left( \epsilon (G_E^p G_E^s)^2 + \tau (G_M^p G_M^s)^2 \right) / D, \quad 13.$$

$$A_{ax} = \epsilon' (1 - 4 \sin^2 \theta_W)^2 G_M^p G_A^e / D, \quad \text{and} \quad 14.$$

$$D = \epsilon (G_E^p)^2 + \tau (G_M^p)^2. \quad 15.$$

The kinematic factors  $\epsilon$  and  $\epsilon'$  (defined in Equation 3) have numerical values close to 1 and 0, respectively, near the forward-angle kinematics of the  $Q_{\text{weak}}$  experiment. As noted in Section 1.2, in this forward-angle limit the asymmetry in Equation 11 can be expressed as in Equation 4, similar to the slope-intercept form of a line  $y(x) = mx + b$ , where  $y(x) = A/A_0$  (both  $A$  and  $A_0$  are functions of  $x = Q^2$ ), the intercept  $b = Q_W^p$ , and the slope  $m = B(Q^2, \theta)$  is itself a function of  $x = Q^2$ :

$$A/A_0(Q^2) = Q_W^p + Q^2 B(Q^2, \theta). \quad 16.$$

The intercept  $Q_W^p$  is a fundamental property of the proton, and so is independent of  $Q^2$ . The slope  $B(Q^2, \theta)$  encapsulating the nucleon structure in terms of the neutron and proton electromagnetic form factors  $G_{E,M}^{p,n}$ , weak neutral form factors  $G_{E,M}^s$  and  $G_A$  described in Equations 12-15 is constrained by PVES data at higher  $Q^2$ . As noted in Section 1.2, it is suppressed relative to  $Q_W^p$  at lower  $Q^2$ , and the asymmetry  $A$  decreases with  $Q^2$  while the elastic scattering cross section increases as  $(1/Q^2)^2$ . The global fit method uses Equation 11 to determine  $Q_W^p$  from the intercept of a fit of  $A/A_0$  vs  $Q^2$ . Therefore asymmetry measurements at lower  $Q^2$  have the advantage that the extrapolation to the intercept at  $Q^2 = 0$  is shorter and the experiment's rates are higher, although the asymmetries are smaller and more challenging to measure.

The result of the global fit reported in (8) is shown in **Figure 4a**. To make this figure tractable, the  $\vec{e}p$  reduced asymmetries were "rotated" to  $\theta = 0^\circ$  as described in (32). The fit varied six parameters:  $C_{1u}, C_{1d}, G_A^p, G_A^n$ , and the overall magnitudes  $\rho_s$  and  $\mu_s$  of the strange electric and magnetic form factors  $G_E^s$  and  $G_M^s$ . The small isoscalar combination of

the axial form factors  $G_A^{Z(T=0)} = (G_A^p + G_A^n)/2$  was constrained by the calculation of (34), leaving five effective parameters in the fit. A dipole form  $G_D = (1 - Q^2/\lambda^2)^{-2}$  with  $\lambda = 1$  GeV<sup>2</sup> was used to describe the  $Q^2$  dependence of  $G_A$ . The strange form factors were taken to be  $G_E^s = \rho_s Q^2 G_D$  and  $G_M^s = \mu_s G_D$  following the work of (48). The fit was truncated at  $Q^2 = 0.63$  GeV<sup>2</sup> in order to avoid nearly doubling the  $Q^2$  reach just to include two additional asymmetries (25) at  $Q^2 = 0.79$  & 1.00 GeV<sup>2</sup> with large uncertainties, which have negligible impact on the outcome of the fit.

The intercept of the global fit,  $Q_W^{gf}(p) = 0.0719 \pm 0.0045$  agrees well with the SM prediction  $Q_W^{SM}(p) = 0.0711 \pm 0.0002$  found in Table 10.4 of (35). Note that the SM prediction of  $Q_W^p$  has improved slightly relative to that reported in (8) due to recent improvements in our knowledge of (mainly) the masses of the top quark and the Higgs boson (35).

An energy-dependence is implicit in  $B(Q^2, \theta)$  since  $Q^2 \sim 4E_f E_i \sin^2 \theta/2$ . As a result, the energy-dependence of the one electroweak radiative correction that depends on energy (the  $\square_{\gamma Z}$ ) has to be accounted for. As described in (32, 8), the  $\bar{e}p$  reduced asymmetries  $A/A_0$  in the PVES database are corrected for the energy-dependence of the vector (36) (the largest piece), and axial-vector (37, 38) pieces of the  $\gamma Z$ -box radiative correction  $\square_{\gamma Z}^{V,AV}$ , as well as a small  $Q^2$  correction (44) to  $\square_{\gamma Z}$ . At the kinematics of the  $Q_{\text{weak}}$  experiment, the combined correction is 0.0046(5), or 6.4%  $\pm$  0.6% of  $Q_W^p$ . Several theoretical groups (39, 40, 41, 42, 43) employing slightly different approaches and experimental constraints generally agree on the central value of  $\square_{\gamma Z}^V$  at the kinematics of the  $Q_{\text{weak}}$  experiment, but differ on the theoretical uncertainty of this correction, as shown in **Figure 3a**. Despite several workshops (45) dedicated to resolving the predicted discrepancies, to date no consensus has been achieved. However, at the present level of uncertainty achieved for  $Q_W^p$ , the differences in the various calculations of the  $\square_{\gamma Z}$  correction and its uncertainty correspond to negligible changes in the result quoted for  $Q_W^p$ . This conclusion was arrived at by carrying out global fits employing each of the  $\gamma Z$ -box predictions in turn, and plotting the results for each in **Figure 3b**.

Reference (8) also explored what happens when the strange form factors  $G_{E,M}^s$  are constrained to the predictions of lattice quantum-chromodynamics (LQCD) calculations (46) instead of being floated in the fit to the PVES data. This reduces the number of effective parameters in the global fit from five to three. The motivation for this is threefold. First, the LQCD calculations have improved to the point that they're near (46) or even at (47) the physical pion mass. The uncertainties for  $G_{E,M}^s$  reported in the LQCD calculations are tiny (more than 20 times smaller than what we can currently determine from fits to experimental data). Second, the best experimental constraints on  $G_{E,M}^s$  come from the higher  $Q^2$  data in the PVES database where  $G_{E,M}^s$  are largest. But those data have larger uncertainties in general than those at lower  $Q^2$ , and are subject to fundamentally different backgrounds which the experiments had to take into account (25), such as hyperon production and decay. Finally, we know already from (46) that there is slight tension at roughly the 1  $\sigma$  level between the strange form factors extracted either from the PVES data or from LQCD calculations. Not knowing a priori which is more appropriate, we explore both.

With  $G_{E,M}^s$  constrained to the LQCD predictions (and uncertainties), the global fit returns  $Q_W^{LQCD}(p) = 0.0685 \pm 0.0038$ . This shift of 0.0034 from the primary  $Q_{\text{weak}}$  result  $Q_W^{gf}(p)$  amounts to a shift of 0.58 $\sigma$  (0.76 $\sigma$ ) assuming the uncertainties are completely uncorrelated (correlated), consistent with the same level of tension apparent in (46). The smaller uncertainty in the  $Q_W^{LQCD}(p)$  result is due to the dramatically smaller  $G_{E,M}^s$  uncertainties in the LQCD  $G_{E,M}^s$  calculations relative to those determined from the PVES data in the global fit. Interestingly, the shape of  $G_{E,M}^s$  (the  $Q^2$  dependence) calculated from the lattice

looks very similar to that assumed for the global fit, which was explored and optimized in a much earlier work (48). The magnitude of both  $G_E^s$  and  $G_M^s$  in the LQCD calculations is about ten times smaller than that determined from the global fit, but the behaviour with  $Q^2$  is about the same.

### 3.2. Determining $Q_W^p$ from the $Q_{\text{weak}}$ Datum & Calculated Form Factors

In the global fit discussed above, the record-breaking precision and proximity to  $Q^2 = 0$  of the  $Q_{\text{weak}}$  experiment's final result clearly dominates the outcome of the fit. The fit is essentially forced to go through the very precise  $Q_{\text{weak}}$  datum, although the slope at that point is determined from the higher  $Q^2$  PVES data. With that in mind, it's interesting to ask the question: what  $Q_W^p$  would result from using the  $Q_{\text{weak}}$  datum *by itself*?

Without the benefit of the other data in the PVES database to determine the hadronic structure  $B(Q^2, \theta)$  term in Equation 16, that term would instead have to be calculated in order to interrogate the  $Q_W^p$  implied from the  $Q_{\text{weak}}$  datum alone. However, extrapolation to  $Q^2=0$  would be unnecessary, since from Equation 16 it's obvious that  $Q_W^p = Q^2 B(Q^2, \theta) - A/A_0(Q^2)$ . In other words, the two terms on the right side of the equation (which each depend on  $Q^2$ ) must conspire to give the  $Q^2$ -independent result ( $Q_W^p$ ) on the left side of the equation.

Further motivating the effort to extract  $Q_W^p$  from the  $Q_{\text{weak}}$  result alone is the fact that at the low  $Q^2$  of the  $Q_{\text{weak}}$  experiment ( $Q^2 = 0.0248 \text{ GeV}^2$ ), the contributions from  $A_s$  and  $A_{ax}$  to the  $B(Q^2, \theta)$  term are small. In (8),  $A_{E,M}$  were taken from the parameterization of the nucleon electromagnetic form factors  $G_{E,M}^{p,n}$  in (33). The  $A_{E,M}^s$  terms were formed from the LQCD calculations of  $G_{E,M}^s$  referred to above from (46). The axial piece  $A_{ax}$  was calculated using the prescription and input for  $G_A$  found in (49). The theoretical uncertainties reported in those three articles were taken fully into account in this "stand-alone" determination of  $Q_W^p$  from the  $Q_{\text{weak}}$  datum. For example, the uncertainty in  $A_E^s$  at each  $Q^2$  is

$$\Delta A_E^s = \sqrt{\left(\frac{\partial A_E^s}{\partial G_E^p}\right)^2 (\Delta G_E^p)^2 + \left(\frac{\partial A_E^s}{\partial G_E^s}\right)^2 (\Delta G_E^s)^2 + \left(\frac{\partial A_E^s}{\partial G_M^p}\right)^2 (\Delta G_M^p)^2}, \quad 17.$$

where the derivatives were taken using Equation 13, and the  $Q^2$ -dependent form factor uncertainties were taken from (33) and (46) for  $\Delta G_{E,M}^p$  and  $\Delta G_E^s$ , respectively. The correction applied for the energy-dependence of the  $\gamma Z$ -box radiative correction (and its uncertainty) was the same as described above in Section 3.1. Each of these contributions to  $Q^2 B(Q^2, \theta)$  was calculated at the  $Q^2$  of the  $Q_{\text{weak}}$  experiment and the results are tabulated in **Table 1**.

The result is  $Q_W^{sa}(p) = 0.0706 \pm 0.0047$ , where the superscript "sa" refers to this "stand-alone" determination using just the  $Q_{\text{weak}}$  datum. It lies just  $0.2\sigma$  below the primary result reported in Section 3.1. Since it makes use of the lattice  $G_{E,M}^s$ , the result might be expected to drop because that's what happened when the lattice results for  $G_{E,M}^s$  were used in the global fit. The reason the drop in  $Q_W^p$  is smaller for the "stand-alone" result than it was for the global fit is likely due to the fact that  $G_{E,M}^s$  is smaller at the  $Q^2$  of the  $Q_{\text{weak}}$  result than it is for any other datum in the PVES database. It's also worth noting of course that the uncertainty of the  $Q_W^p$  result extracted from the  $Q_{\text{weak}}$  experiment's datum alone is almost the same as that extracted using the global fit and the entire PVES database.

One advantage of the stand-alone result is its simplicity and transparency. It's easy to use **Table 1** to estimate the impact on  $Q_W^p$  from various effects. One such effect of

contemporary interest is the “proton-radius puzzle” (?), so-named because the proton radius determined from electron-scattering data disagrees by up to seven standard deviations from that determined from muonic Lamb-shift measurements. Since the determination of  $Q_W^p$  relies on our knowledge of  $G_E^p$  and therefore indirectly on  $r_p = \langle r_E^2 \rangle^{1/2}$  it’s reasonable to ask what impact this ambiguity in  $r_p$  has on the determination of  $Q_W^p$ . There are many different experiments available to characterize the magnitude of the proton radius puzzle, but two typical examples are an electron-scattering-data global-analysis (50) which finds  $r_p(ep) = 0.875 \pm 0.010$  fm, and a muonic Lamb-shift result (51) which returns  $r_p(\mu p) = 0.8409 \pm 0.0004$  fm. The difference  $\Delta r_p = 0.034$  fm, or  $3.4\sigma$ . The impact of this on  $Q_W^p$  can be estimated from the familiar  $Q^2 \rightarrow 0$  Taylor series expansion

$$G_E \sim Z(1 - Q^2 \langle r^2 \rangle / 6 + \dots). \quad 18.$$

This equation says that at the small  $Q^2$  of the  $Q_{\text{weak}}$  experiment, the two different values of  $r_p$  imply  $G_E(ep) \sim 0.9178$  and  $G_E(\mu p) \sim 0.9241$ , i.e. a  $\Delta G_E = 0.7\%$ . According to **Table 1**,  $G_E$  contributes  $-26.2$  ppb to the hadronic structure asymmetry, so the shift in asymmetry implied by the proton radius puzzle is  $\Delta A \sim (0.7\%)(26 \text{ ppb}) \sim 0.2$  ppb out of the  $-226.5$  ppb measured in that experiment. Then the estimated shift in  $Q_W^p$  due to the proton radius puzzle is  $\Delta Q_W^p \sim \Delta A/A_0 = 0.00008$ , or 2% of the  $Q_{\text{weak}}$  uncertainty (only 0.1% of the  $Q_{\text{weak}}$  central value). We can therefore conclude that the effect of the proton-radius puzzle on the determination of  $Q_W^p$  is completely negligible.

Another effect apparent from **Table 1** which is pertinent to future higher-precision experiments is the size of the uncertainties associated with the hadronic-structure contributions. In this table, the contributions from  $A_{E,M}^{p,n}$ ,  $A_{E,M}^s$  and  $A_{ax}$  are added in quadrature. But the contributions from the uncertainties in  $G_E^p$ ,  $G_E^n$ ,  $G_M^p$ , and  $G_M^n$  which contribute to  $A_{E,M}^{p,n}$  are also assumed to be uncorrelated because the correlations are not reported in the literature. Therefore the uncertainties associated with the EM form factors  $A_{E,M}^{p,n}$  are overestimated in the stand-alone method.

In the global fit described above in Section 3.1, this problem was dealt with (8) by performing the fit with a variety of different EM form factor parameterizations (33, 52, 53, 54) and folding the full range of variation observed in  $Q_W^p$  into the uncertainty of the weak charge result. That estimation of the uncertainty associated with the EM form factors was about 1%, only a small additional contribution to the uncertainty reported in the  $Q_{\text{weak}}$  experiment.

### 3.3. $Q_W^p$ from the $Q_{\text{weak}}$ Datum, PVES Database & Calculated Form Factors

The successful extraction of the weak charge described above using just the  $Q_{\text{weak}}$  datum leads one to ask whether this technique could be extended to the entire PVES database. What Section 3.2 essentially found is that since  $Q_W^p$  is independent of  $Q^2$ , it can be determined from *any* datum in the PVES database. Obviously the place to start is with the datum closest to threshold and with the highest precision. But in this section we explore what happens if we determine a  $Q_W^p$  for each measured asymmetry in the PVES database by calculating  $(A_{E,M})$ ,  $A_{E,M}^s$ , and  $A_{ax}$  for each datum, and fitting the resulting weak charges with a straight line as a function of  $Q^2$ . Since the  $Q_W^p$  determined in this manner for each datum should be the same number (within our ability to calculate the hadronic structure terms  $A_{E,M}^s$  and  $A_{ax}$ ), the fit should be a straight line with a small and constant slope. This would stand in contrast to the situation for the global fit described in Section 3.1

where the fit had a relatively steep slope, especially in the extrapolation region.

In Section 3.1 it was important to include the  $\bar{e}d$  data (26, 23, 24, 19) to constrain  $A_{ax}$ , and to include  $\bar{e}^4\text{He}$  data (30, 29) to constrain  $A_E^s$  in particular, when fitting the PVES data which are mostly comprised of  $\bar{e}p$  elastic asymmetries. But since we're going to calculate  $A_{ax}^s$  and  $A_{E,M}^s$  for this linear-fit method, those data aren't as helpful. They mostly measure the neutron's weak charge and aren't very sensitive to the much smaller proton weak charge. Using the same lattice calculations and axial calculations as employed in Section 3.2, the weak charges determined from each datum in the  $\bar{e}p$  database (25, 26, 27, 28, 30, 31, 20, 21, 22, 23) are plotted in **Figure 4(b)**, along with the linear fit to these results. The more precise of the two  $\bar{e}^4\text{He}$  results is also included but has negligible impact on the fit. It's apparent from this figure that the slope of the fitted line is reasonably shallow relative to the global fit in **Figure 4(a)**. The intercept of the fit is  $Q_W^{sl}(p) = 0.0689 \pm 0.0045$ , where the superscript "sl" denotes the straight-line fit. This agrees almost exactly with the lattice result obtained in the global fit:  $Q_W^{LQCD}(p) = 0.0685 \pm 0.0038$ .

Both the "sl" and "LQCD" results are  $0.6\sigma$  lower than the global fit, whereas the "sa" (stand-alone) fit is only  $0.2\sigma$  lower. This supports the explanation that the  $G_{E,M}^s$  in the higher  $Q^2$  PVES data are what's dragging down the result in the "sl" and "LQCD" results. There appears to be some slight tension between the fit-strange and lattice-strange form factors at higher  $Q^2$ .

#### 4. The Running of $\sin^2 \theta_w$

The most convenient way to compare precision neutral-current measurements is through values of the weak mixing angle,  $\sin^2 \theta_w$ , extracted from each measurement. The weak mixing angle characterizes the mixing of the two neutral currents (electromagnetic and neutral weak) in the SM. Neutral-current experiments have measured the decays of directly-produced  $Z^0$  bosons at or near the  $Z^0$  mass and also the effects of virtually-exchanged  $Z^0$  bosons at energy scales well below the  $Z^0$  mass. Expressions for each of the experimental observables that include all quantum corrections at the one-loop level can be used to extract a value of  $\sin^2 \theta_w$  for each measurement. Details of this extraction procedure for the  $Q_{\text{weak}}$  experiment can be found in Reference (8). The extracted values for the most precise measurements at and below the  $Z^0$  mass are shown in **Figure 5**. The theoretical prediction for how  $\sin^2 \theta_w$  evolves with energy scale  $Q$  - often referred to as the "running of the weak mixing angle" - is shown as the dark curve (55, 56, 57) in **Figure 5**. This evolution from the  $Z$ -pole is calculated using the renormalization-group-equation procedure in the modified-minimal-subtraction ( $\overline{MS}$ ) scheme. The relative theoretical-precision of this curve is  $\pm 0.01\%$  at  $Q$  corresponding to the  $Z$  boson mass from a global fit to the SM, with an additional evolution uncertainty from hadronic effects of  $\pm 0.01\%$  at  $Q = 0$  (56).

The  $Z^0$  pole measurements (35) in **Figure 5** come from several measurements at LEP1, with the forward-backward asymmetry  $A_{FB}$  from  $Z \rightarrow b\bar{b}$  being the most precise, the left-right  $Z$  pole production asymmetry  $A_{LR}$  measurement at the SLC, and forward-backward asymmetry measurements of Drell-Yan lepton pairs at the Tevatron and LHC. The most precise measurements at low energy are all weak-charge measurements, with the  $Q_{\text{weak}}$  measurement completing the "weak charge triad" (58). This includes the weak-charge measurements of the electron in PV Møller scattering (E158) (7),  $^{133}\text{Cs}$  (dominated by the weak charge of the neutron) from atomic PV (59, 60), and the proton from  $Q_{\text{weak}}$  (8).

Both the weak charge of the electron and the proton are suppressed in the SM (both

( $1 - 4 \sin^2 \theta_W$ ) to first order), while the weak charge of  $^{133}\text{Cs}$ , which is dominated by the neutron's weak charge, has no such suppression. The consequence of this is that a much more precise relative uncertainty on the  $^{133}\text{Cs}$  measurement is required for similar precision on the weak mixing angle. Specifically, relative precision on the weak-charge measurements of 13%, 6.3%, and 0.59% for the electron, proton, and  $^{133}\text{Cs}$  are required for relative precision on  $\sin^2 \theta_W$  of 0.54%, 0.47%, and 0.81%, respectively. Within the precision of these measurements, the SM predicts a constant value of the weak mixing angle in this low energy region. Testing the hypothesis that these three measurements are consistent with a constant results in a chi-squared per degree of freedom of 1.90 corresponding to a probability of 0.149. Thus, it is reasonable to combine the points to obtain the weighted-average point shown in **Figure 5**. The predicted SM running of  $\sin^2 \theta_W$  from the  $Z$ -pole to  $Q = 0$  is a relative change of about 3.2%. Using the weighted-average value, this change is confirmed with  $9.6 \sigma$  significance.

All of the measurements are consistent at the  $< 2\sigma$  level with the SM with the exception of the NuTeV result (61) from neutrino-nucleus scattering. It has been argued (62) that some of the cause for this  $3 \sigma$  discrepancy is substantial unaccounted-for nuclear-physics effects, including neutron-excess corrections to the quark momenta, charge-symmetry breaking, and strange-quark momentum-asymmetries. When estimates of these effects are included, the  $\sin^2 \theta_W$  value from NuTeV comes into agreement with the SM prediction.

The most precisely determined data points in **Figure 5** are from the  $Z$ -pole. However, the low-energy points with more modest precision have better sensitivity to certain types of BSM physics due to the fact that they are well away from the  $Z$ -pole. This includes effects due to heavy new-physics such as additional heavy  $Z'$  bosons, or leptoquarks, that can generally be described by an effective low-energy four-fermion contact interaction as discussed in Section 5. The contribution of such interactions is heavily suppressed at the  $Z$ -pole, due to the lack of an interference term (63). This can be understood by inspecting the amplitudes for the exchanges of a  $Z$ -boson and new physics characterized by an exchange particle of mass  $\Lambda$  and decay width  $\Gamma_{new}$ :

$$A_Z \propto \frac{1}{q^2 - M_Z^2 + iM_Z\Gamma_Z} \quad A_{new} \propto \frac{1}{q^2 - \Lambda^2 + i\Lambda\Gamma_{new}} \quad 19.$$

At the  $Z$ -pole ( $q^2 = M_Z^2$ ),  $A_Z$  is purely imaginary and the new physics amplitude is dominantly real in the situation where  $\Lambda \gg M_Z, \Gamma_{new}$ . There is then no interference term between the  $Z$  and new physics terms in the amplitude:

$$|A_Z + A_{new}|^2 = A_Z^2 \left[ 1 + \left( \frac{A_{new}}{A_Z} \right)^2 + \dots \right]. \quad 20.$$

On the other hand, at low energies ( $q^2 \ll M_Z^2$ ), both amplitudes are dominantly real and there is an interference term:

$$|A_Z + A_{new}|^2 = A_Z^2 \left[ 1 + 2 \left( \frac{A_{new}}{A_Z} \right) + \dots \right]. \quad 21.$$

Since we are considering the case  $\Lambda \gg M_Z$  and therefore  $A_{new} \ll A_Z$ , the new physics makes a much larger relative contribution to the observable at low energy than on the  $Z$ -pole.

Future experiments are also shown in **Figure 5**. Improved precision measurements on the weak charges of the proton (64) and electron (65) are planned. In addition there are

plans to improve the existing deep-inelastic scattering datum (66) using a new approach (67, 68). Several efforts are also being pursued for improved atomic parity-violation experiments. A summary can be found in (57).

## 5. The Search for Physics Beyond the Standard Model

The weak charge result can be used to set limits on potential new physics beyond the standard model. In principle, the new physics might not couple to the same "uud" combination of quark flavors found in the proton. In order to allow the new physics to couple to arbitrary (valence)-quark flavors, we define a flavor mixing-angle

$$\theta_h = \tan^{-1}(N_d/N_u) \quad 22.$$

as in (69). For the proton,  $N_d = 1$ ,  $N_u = 2$ , and  $\theta_h = 26.6^\circ$ . Then the "u" and "d" quark components can be expressed as

$$h_V^u = \cos \theta_h, \text{ and } h_V^d = \sin \theta_h. \quad 23.$$

Let  $q$  represent the quark flavor, and  $C_{1q}$  the vector-quark couplings. Then new parity-violating, semi-leptonic four-point contact-interaction BSM physics can be introduced in the Lagrangian in a completely general (model-independent) way with a new contact interaction characterized by mass scale  $\Lambda$  and coupling  $g$ . The measured PV Lagrangian  $\mathcal{L}_{PV}^{msrd}$  can be expressed as the sum of the SM neutral-current Lagrangian  $\mathcal{L}_{NC}^{SM}$  and the PV piece  $\mathcal{L}_{PV}^{new}$  associated with new BSM physics:

$$\mathcal{L}_{PV}^{msrd} = \mathcal{L}_{NC}^{SM} + \mathcal{L}_{PV}^{new} \quad 24.$$

$$= \bar{e}\gamma_\mu\gamma_5 e \sum_q \left( \frac{G_F}{\sqrt{2}} C_{1q} + \frac{g^2}{\Lambda^2} h_V^q \right) \bar{q}\gamma^\mu q. \quad 25.$$

26.

Rearranging and carrying out the sum using Equation 23, we can recast Equation 25 in terms of the vector-quark charges  $C_{1q}$  as follows:

$$\left( C_{1u}^{msrd}, C_{1d}^{msrd} \right) = \left( C_{1u}^{SM}, C_{1d}^{SM} \right) + r (\cos \theta_h + \sin \theta_h). \quad 27.$$

This is just the polar form of a circle in  $C_{1q}$  space centered at the SM value of the vector-quark charges  $(C_{1u}^{SM}, C_{1d}^{SM})$ , with radius

$$r = \frac{\sqrt{2}}{G_F} \left( \frac{g}{\Lambda} \right)^2. \quad 28.$$

These circles describe contours of different mass sensitivity  $\Lambda/g$  in  $C_{1q}$  space, as illustrated in **Figure 6**.

### 5.1. Constraints Provided by Weak Charge Experiments

The constraint (at tree level<sup>1</sup>) provided by the  $Q_{\text{weak}}$  experiment in  $C_{1q}$  space is the band defined by the two lines

$$Q_W(p) \pm \Delta Q_W(p) = -2(2C_{1u} + C_{1d}). \quad 29.$$

<sup>1</sup>See Equation 10.30 in (35) for the full expression including radiative corrections.

The mass reach associated with the  $Q_{\text{weak}}$  experiment alone can be read directly off **Figure 6** or computed geometrically as the distance between the SM origin and the lines defining the perimeter of the  $Q_{\text{weak}}$  band. The distance between the line  $Ax + By + C = 0$  and the point  $(C_{1u}^{SM}, C_{1d}^{SM}) = (-0.18853, 0.34151)$  is

$$d = \frac{AC_{1u}^{SM} + BC_{1d}^{SM} + C}{\pm\sqrt{A^2 + B^2}}, \quad 30.$$

where in the case of  $Q_W(p)$  we have  $A = -4$ ,  $B = -2$ , and  $C = Q_W(p) \pm \Delta Q_W(p) = 0.0719 \pm 0.0045$ , and  $\Lambda/g$  is determined from this distance  $d$  using Equation 28. The larger of these two distances is related via Equation 28 to the minimum mass reach below which new PV SL BSM physics is excluded for the proton by the  $Q_{\text{weak}}$  experiment:  $\Lambda/g = 7.5$  TeV (95% C.L.). For the value (70) of  $g^2 = 4\pi$  typically chosen to make comparisons between different experiments (71), this implies a mass reach of  $\Lambda = 26.6$  TeV (95% C.L.) for the  $Q_{\text{weak}}$  experiment. Note that the slope of the lines defining the  $Q_{\text{weak}}$  band ( $-2$ ) means that the slope of a line perpendicular to the band is  $+1/2$ , which corresponds to the  $\theta_h = 26.6^\circ$  flavor mixing-angle of the proton (see Equation 22).

The intuitive geometrical analysis described above makes use of the measured weak charge and the SM values for the vector weak couplings. Alternatively, precisely the same results may be obtained by comparing the measured and SM values of the weak charge as in (8):

$$\frac{\Lambda_{\pm}}{g} = v \sqrt{\frac{4\sqrt{5}}{|Q_W^p \pm 1.96\Delta Q_W^p - Q_W^{SM}|}}, \quad 31.$$

where  $v = 1/\sqrt{\sqrt{2}G_F} = 0.24622$  TeV is the electroweak (Fermi) scale, and represents the vacuum expectation value of the Higgs field. The lesser of the two values described in Equation 31 is  $\Lambda_+/g = 7.5$  TeV, using  $Q_W^{SM}(p) = 0.0711$  from Table 10.4 in (35). It agrees with the geometric result obtained using Equation 30.

The only other high-precision SL weak charge measurement (59) was performed on cesium ( $^{133}\text{Cs}$ ), although experiments with less precision have also been published for Thallium (73), Bismuth (74) and Lead (75). The atomic parity-violating (APV) results (59, 72, 60) also provide constraints (bands) in  $C_{1q}$  space since for a system of  $Z$  protons and  $N$  neutrons (at tree level), the weak charge can be expressed as (35)

$$Q_W(Z, N) = -2((2Z + N)C_{1u} + (Z + 2N)C_{1d}). \quad 32.$$

Using the most recent atomic corrections (60) to the cesium result (59, 72):

$$Q_W(^{133}\text{Cs}) = -2(188C_{1u} + 211C_{1d}) = -72.62 \pm 0.43. \quad 33.$$

Combining this result with Equation 30 we can determine a mass reach for the  $^{133}\text{Cs}$  APV band the same way we did for the  $Q_{\text{weak}}$  experiment's band. We find the mass reach associated with the  $^{133}\text{Cs}$  APV band is  $\Lambda/g = 6.9$  TeV (95% C.L.).

The combined constraints from  $Q_{\text{weak}}$  (ep) and APV ( $^{133}\text{Cs}$ ) on the vector weak charges  $C_{1u}$  and  $C_{1d}$  are defined by the ellipse

$$\Delta\chi^2 = \left( \frac{Q_W^{APV}(X, Y) - Q_W^{APV}(\text{msrd})}{\Delta Q_W^{APV}(\text{msrd})} \right)^2 + \left( \frac{Q_W^p(X, Y) - Q_W^p(\text{msrd})}{\Delta Q_W^p(\text{msrd})} \right)^2. \quad 34.$$

Here  $\Delta\chi^2 = 5.99$  for 95% CL (see Table 39.2 in (35)).  $Q_W^{APV}(X, Y)$  and  $Q_W^p(X, Y)$  refer to Equation 32 for  $^{133}\text{Cs}$  (APV) and the proton ( $Q_{\text{weak}}$ ) with  $(X, Y) = (C_{1u}, C_{1d})$ . The values  $Q_W(\text{msrd})$  and uncertainties  $\Delta Q_W(\text{msrd})$  of the weak charges measured for  $^{133}\text{Cs}$  and the proton are taken from Table 10.4 of (35). The 95% C.L. constraints (bands) defined by the  $Q_{\text{weak}}$  and APV weak charge measurements, as well as the 95% C.L. ellipse defined by combining both bands is shown along with different  $\Lambda/g$  contours in **Figure 6**.

## 5.2. Flavor-independent Constraints

The mass reaches quoted so far for  $Q_{\text{weak}}$  (ep) and APV ( $^{133}\text{Cs}$ ) are specific to the proton and  $^{133}\text{Cs}$ , respectively. But there is no reason to assume that the new and unknown BSM physics would necessarily couple to the specific flavor ratios of those two systems. The new physics might only couple to "u" quarks, or only "d", or some other combination. To obtain a completely general result, we seek a mass reach that's independent of what flavors the new physics couples to.

The ellipse in **Figure 6** shows the most likely region at 95% confidence level to find any of a generic class of BSM physics models parameterized by  $\Lambda/g$  and  $\theta_h$ . It's tempting to associate the point on this ellipse farthest from the SM origin with the minimum  $\Lambda/g$  for any given  $\theta_h$ , in other words, a  $\theta_h$ -independent mass limit for BSM physics. But the ellipse is by definition a 2-parameter entity, and we seek a 1-parameter solution. Once we pick a  $\theta_h$ , we are just considering a single slice through the parameter space.

Mass limits appropriate to a specific choice of the flavor-mixing angle  $\theta_h$  can be obtained by considering a line of constant  $\theta_h$  through the SM origin. Since only the parameter  $\Lambda/g$  varies along fixed  $\theta_h$ , the distance from the SM origin (radius) along this line corresponding to  $\Delta\chi^2 = 3.84$  about the local  $\chi^2$  minimum is the 95% CL limit on  $\Lambda/g$  for that particular value of  $\theta_h$ . In practice, we pick a specific  $\theta_h$  and proceed as follows: First the radius  $r_{\text{min}}$  associated with the local  $\chi^2$  minimum  $\chi_{\text{min}}^2(\theta_h)$  is identified by setting the derivative  $\partial(\Delta\chi^2)/\partial r$  of Equation 34 to zero with  $(X, Y) = (r \cos \theta_h, r \sin \theta_h)$ . We then obtain  $\chi_{\text{min}}^2(\theta_h)$  from Equation 34 with  $(X, Y) = (r_{\text{min}} \cos \theta_h, r_{\text{min}} \sin \theta_h)$ . Then Equation 34 is solved for  $r$  with  $\Delta\chi^2 = (\chi_{\text{min}}^2(\theta_h) + 3.84)$  at the specific  $\theta_h$  under consideration. That radius corresponds to a 95% CL  $\Lambda/g$  for that choice of  $\theta_h$  via Equation 28. Carrying out this procedure for all values of  $\theta_h$  results in the mass-limit curve as a function of  $\theta_h$  shown in **Figure 7(a)**. The minimum  $\Lambda/g$  on that curve is 3.6 TeV, the  $\theta_h$ -independent  $\Lambda/g$  mass limit below which the combined constraints from  $Q_{\text{weak}}$  and APV rule out PV SL 4-point contact-interaction BSM physics. For the usual benchmark  $g^2 = 4\pi$ , this flavor-independent mass limit is  $\Lambda = 12.6$  TeV.

It is worth noting that an approximation to the rigorous procedure discussed above for determining this flavor-independent result for  $\Lambda/g$  can be achieved to within about 0.1 TeV by simply finding the point on the combined ellipse of Equation 34 farthest from the SM origin, and converting that distance to a mass reach using Equation 28. This is a unique consequence of the fact that the  $Q_{\text{weak}}$  result (and to a lesser extent the APV result) is in such good agreement with the SM.

## 5.3. Constraints on Specific BSM Extensions

Above we expressed the sensitivity of the  $Q_{\text{weak}}$  experiment to new BSM physics in terms of  $\Lambda/g$  in order to remain independent of the specific choice of coupling  $g$  associated with the new physics. As mentioned above, however, it is conventional to compare the mass

reach of different experiments (71) using the specific coupling  $g^2 = 4\pi$  (70) associated with compositeness (76). Compositeness posits that quarks and leptons have internal structure. Following this tradition, the  $Q_{\text{weak}}$  experiment has a mass reach  $\Lambda = 26.6$  TeV (95% CL). The previous best SL (eeqq) mass reach for compositeness was 24 TeV (77), also 95% CL.

However,  $g^2 = 4\pi$  is on the high end of coupling strengths assumed for BSM physics. Perhaps a more natural size is  $g \sim 1$ , as is the case for the couplings of the known bosons. It could be even smaller. For example, a coupling strength of  $g^2 = 4\pi\alpha$  is usually assumed for leptoquarks (78). Leptoquarks are theoretically postulated particles which have both lepton and baryon numbers, and arise in SM extensions like technicolor and GUTs. The mass reach provided by the  $Q_{\text{weak}}$  result for leptoquarks (assuming  $g^2 = 4\pi\alpha$ ) is only  $\Lambda = 2.3$  TeV. That still improves on the existing 95% CL leptoquark mass reach of 1.755 TeV (79).

## 6. Future Prospects

There are two separate aspects to consider in order to evaluate the prospects of future experiments to measure the proton's weak charge: overcoming the experimental challenges, and assessing the impact on raising the mass reach for BSM physics.

### 6.1. Experimental Challenges

The  $Q_{\text{weak}}$  result was statistics dominated:  $A_{\text{ep}} = -226.5 \pm 7.3$  (statistics)  $\pm 5.8$  ppb (systematics). It required roughly 1 year of production running spread over 2 years. The first three of the  $Q_{\text{weak}}$  experiment's systematic uncertainties listed in **Table 2** made up 2/3 of the total systematic error. If the  $Q_{\text{weak}}$  experiment were to be repeated, it would certainly be feasible to reduce many of the systematic uncertainties, but improving the total systematic uncertainty by more than a factor of 2-3 seems doubtful without significant changes to the kinematics, the apparatus, and the measured beam properties.

The P2 experiment (64), which aims to measure the proton's weak charge in a challenging experiment at a new facility (MESA) located in Mainz, Germany has significant differences compared to the  $Q_{\text{weak}}$  experiment. The current P2 reference design (64) would employ 150  $\mu\text{A}$  of 155 MeV longitudinally-polarized electrons on a 60 cm-long LH2 target at a mean angle of  $35^\circ$  and at a  $Q^2$  of only 0.0045  $\text{GeV}^2$ . The goals of the P2 experiment are to measure the expected  $-40$  ppb asymmetry to 1.4% ( $\pm 0.5$  ppb (stat)  $\pm 0.25$  ppb (syst)), the proton's weak charge to 1.5% ( $\pm 0.0011$ ), the weak mixing-angle to 0.14% ( $\pm 0.00033$ ), and the mass reach  $\Lambda/g$  to 13.8 TeV (49 TeV with  $g^2 = 4\pi$ ). Their strategy for achieving these ambitious goals is detailed in (64).

The absolute statistical uncertainty achievable in the P2 experiment benefits relative to that achieved in the  $Q_{\text{weak}}$  experiment from the higher  $ep$  elastic scattering cross section at their 5.5 times lower  $Q^2$ , their longer target and larger solid angle acceptance. As shown in Equation 5, the resulting smaller asymmetry reduces the figure of merit, but the tradeoff with the smaller absolute statistical error results in a proposed fractional statistical uncertainty of 1.3%, which is a factor of 2.3 improvement over  $Q_{\text{weak}}$ . Keeping the asymmetry statistical width close to the counting statistics limit will remain a challenge: other random noise sources such as target noise, BCM width, detector resolution, and deadtimes from helicity switching and detector-signal processing must all be controlled better than they were in the  $Q_{\text{weak}}$  experiment.

The P2 requirements for the total fractional and absolute systematic uncertainty are, respectively, a factor of 4 and 23 more demanding than what  $Q_{\text{weak}}$  achieved. Systematic uncertainties associated with normalization factors such as beam polarization are similar to what  $Q_{\text{weak}}$  achieved. However, P2 cannot employ the Compton polarimetry technique due to the low beam energy, so they are developing a Møller polarimeter with trapped polarized-hydrogen atoms instead. Other systematic uncertainties, such as those from the beam-current-monitors (BCM), the beamline background, the HCBAs, and some types of backgrounds were among the largest contributions to the systematic uncertainty in the  $Q_{\text{weak}}$  experiment. The P2 goals for these represent a significant improvement over both the  $Q_{\text{weak}}$  fractional and absolute systematic uncertainties. For example, differences in the relative beam charges measured in the three BCMs used during the majority of the  $Q_{\text{weak}}$  experiment required the assignment of a 2.6 ppb systematic error.

## 6.2. Interpretability Challenges

In this section we focus on improvements to the mass reach for BSM physics that might be achieved in future experiments. The present limits and how they were arrived at were discussed in detail in Section 5. Those results include the mass reach on the proton set by the  $Q_{\text{weak}}$  experiment, as well as the flavor-independent mass reach provided by the combined results of the  $Q_{\text{weak}}$  experiment and the APV experiment on cesium. Now we explore how each of these constraints might be improved with possible new experiments.

Using Equation 31 from Section 5, we show in **Figure 8** how the 95% CL mass reach on the proton depends on the uncertainty  $\Delta Q_W^p$  attained in a measurement of  $Q_W^p$ . This figure assumes a central value for  $Q_W^p$  on the SM, as well as  $\pm\Delta Q_W^p$  off the SM at each  $\Delta Q_W^p$ . The P2 experiment’s proposed goal of  $\Delta Q_W^p = 0.0011$  is about 4 times better than the precision achieved in the  $Q_{\text{weak}}$  experiment, and thus nominally twice the mass reach achieved in the  $Q_{\text{weak}}$  experiment. Depending on where the P2 central value for  $Q_W^p$  falls within  $\pm 1\sigma$  (i.e.  $\pm 0.0011$ ) of the SM, the figure shows that the P2 mass reach  $\Lambda_+$  (see Equation 31 with  $g^2 = 4\pi$ ) could range anywhere from 46 to 80 TeV. This would constitute a significant improvement over the present limit of 26.6 TeV set by the  $Q_{\text{weak}}$  experiment.

Improving the flavor-independent mass reach is a much heavier lift, because the present limit (Section 5.2) is already based on two precise experiments: both the cesium APV result as well as the  $Q_{\text{weak}}$  result. We explore what the likely discovery space is for future  $Q_W^p$  experiments in **Figure 7(b)**, as well as future APV experiments on cesium in **Figure 7(c)**, or both in **Figure 7(d)**. In each panel we show the existing 95% CL  $\Lambda/g$  constraint as a function of the flavor-mixing angle  $\theta_h$ , and then add additional experiments with the same, half, or quarter the uncertainty of the existing experiments. We assume each new experiment’s central value falls on the SM, and follow the same procedure detailed in Section 5.2 except with the appropriate additional terms added to Equation 34. The resulting minimum  $\Lambda/g$  represents the mass limit below which PV SL 4-point contact interaction BSM physics is excluded *independent* of what quark flavors the new physics couples to. With a new  $Q_W^p$  measurement from P2 assuming a central value on the SM and assuming the  $\pm 0.0011$  uncertainty proposed for that experiment, combined with the existing  $Q_{\text{weak}}$  and APV cesium results, the  $\theta_h$ -independent mass reach  $\Lambda/g$  would improve from 3.6 TeV to 4.2 TeV. The improvement in the  $\theta_h$ -independent mass reach that could be achieved with new  $Q_W^p$  experiments, or with new APV experiments, is relatively modest compared to the improvement that could be achieved with both together.

## 7. Summary

A solid foundation of expertise and knowledge acquired starting with the earliest PV experiments at Los Alamos and SLAC, then later at TRIUMF, PSI, MIT/Bates, Mainz, and Jefferson Lab has made it possible to measure the PV ep asymmetry with the ppb-scale precision necessary to determine the proton's weak charge  $Q_W^p$  for the first time. These earlier experiments not only incrementally taught the PV community how to do these challenging measurements, but also provided the hadronic structure information needed to extract the weak charge from the precise  $Q_{\text{weak}}$  experiment's asymmetry measurement ( $A_{ep} = -226.5 \pm 9.3$  ppb) targeted near threshold at  $Q^2 = 0.00248$  GeV<sup>2</sup>. The result of this decades-long effort was a 6.3% measure of  $Q_W^p = 0.0719 \pm 0.0045$ , which is in close agreement with the SM value  $Q_W^p = 0.0711 \pm 0.0002$ . Some of the most relevant aspects of this  $Q_{\text{weak}}$  experiment were described. We explained in detail how consistent results for the proton's weak charge are extracted using several different methods employing varying degrees of input from data and calculated form factors. The resulting  $Q_W^p$  has been used to determine the most precise measure of the weak mixing-angle below the Z-pole,  $\sin^2 \theta_W(Q = 0.158 \text{ GeV}) = 0.2382 \pm 0.0111$ , and compared it to determinations from other experiments. The article then described the  $\Lambda/g = 7.5$  TeV mass reach determined at 95% CL from the  $Q_{\text{weak}}$  result for BSM physics on the proton, as well as for any combination of quark flavors by including the APV result on cesium:  $\Lambda/g = 3.6$  TeV. With the usual  $g^2 = 4\pi$  associated with compositeness and commonly used for comparisons with other experiments, these mass limits correspond to  $\Lambda = 26.6$  TeV and  $\Lambda = 12.6$  TeV, respectively. Finally, the impact new experiments could have on these mass limits was explored. The community looks forward to a bright future from the next generation of experiments.

## DISCLOSURE STATEMENT

The authors are not aware of any affiliations, memberships, funding, or financial holdings that might be perceived as affecting the objectivity of this review.

## Greg: ACKNOWLEDGMENTS

The authors wish to thank all their collaborators on the  $Q_{\text{weak}}$  experiment, as well as the staffs of Jefferson Laboratory, TRIUMF and the MIT/Bates laboratory. This work was supported by the US Department of Energy (DOE) Contract number DEAC05-06OR23177, under which Jefferson Science Associates, LLC, operates the Thomas Jefferson National Accelerator Facility. Construction and operating funding for the  $Q_{\text{weak}}$  experiment was provided through the US DOE, the Natural Sciences and Engineering Research Council of Canada (NSERC), the Canadian Foundation for Innovation (CFI), and the National Science Foundation (NSF) with university matching contributions from the College of William and Mary, Virginia Tech, George Washington University and Louisiana Tech University.

## LITERATURE CITED

1. Aad G, et al. (ATLAS Collab.) *Physics Letters B* 716:1 (2012)
2. Chatrchyan S, et al. (CMS Collab.) *Physics Letters B* 716:30 (2012)
3. Erler J, Su S. *Prog. Part. Nucl. Physics* 71:119 (2013)
4. Erler J, et al. *Annu. Rev. Nucl. Part. Sci.* 64:269 (2014)

5. Potter JM, et al. *Phys. Rev. Lett.* 33:1307 (1974)
6. Prescott CY, et al. *Phys. Lett. B* 84:524 (1979)
7. Anthony PL, et al. *Phys. Rev. Lett.* 95:08161 (2005)
8. Androić D, et al. (Qweak Collab.) *Nature* 557:207 (2018)
9. Allison, T, et al. (Qweak Collab.) *Nucl. Instrum. Meth. A* 781:105 (2015)
10. Duvall WS. *Precision Measurement of the Proton's Weak Charge using Parity-Violating Electron Scattering*. PhD Thesis, Va. Polytech. Inst. State Univ. (2017)
11. Myers KE. *The First Determination of the Proton's Weak Charge Through Parity-Violating Asymmetry Measurements in Elastic  $e + p$  and  $e + Al$  Scattering*. PhD Thesis, Geo. Wash. Univ. (2012)
12. Magee JA. *A Measurement of the Parity-Violating Asymmetry in Aluminum and its Contribution to a Measurement of the Proton's Weak Charge*. PhD Thesis, Coll. of Will. and Mary (2016)
13. Bartlett KD. *First Measurements of the Parity-Violating and Beam-Normal Single-Spin Asymmetries in Elastic Electron-Aluminum Scattering*. PhD Thesis, Coll. of Will. and Mary (2018)
14. Kargiantoulakis E. *A Precision Test of the Standard Model via Parity-Violating Electron Scattering in the Qweak Experiment*. PhD Thesis, Univ. Virg. (2015)
15. Jones DC. *Measuring the Weak Charge of the Proton via Elastic Electron-Proton Scattering*. PhD Thesis, Univ. Virg. (2015)
16. Gray VM. *Determination of the Kinematics of the Qweak Experiment and Investigation of an Atomic Hydrogen Møller Polarimeter*. PhD Thesis, Coll. of Will. and Mary (2018)
17. Hauger M, et al. *Nucl. Inst. & Meth. A* 462:382 (2001)
18. Narayan A, et al. *Phys. Rev. X* 6:011013 (2016)
19. Ito TM, et al. (SAMPLE) *Phys. Rev. Lett.* 92:102003 (2004)
20. Spayde DT, et al. (SAMPLE) *Phys. Lett. B* 583:79 (2004)
21. Maas FE, et al. (PVA4) *Phys. Rev. Lett.* 93:022002 (2004)
22. Maas FE, et al. (PVA4) *Phys. Rev. Lett.* 94:152001 (2005)
23. Baunack S, et al. (PVA4) *Phys. Rev. Lett.* 102:151803 (2009)
24. Balaguer Ros D, et al. *Phys. Rev. D* 94:051101 (2016).
25. Armstrong DS, et al. (G0) *Phys. Rev. Lett.* 95:092001 (2005)
26. Androić D, et al. (G0) *Phys. Rev. Lett.* 104:012001 (2010)
27. Aniol KA, et al. (HAPPEX) *Phys. Rev. C* 69:065501 (2004)
28. Aniol KA, et al. (HAPPEX) *Phys. Lett. B* 635:275 (2006)
29. Aniol KA, et al. (HAPPEX) *Phys. Rev. Lett.* 96:022003 (2006)
30. Acha A, et al. (HAPPEX) *Phys. Rev. Lett.* 98:032301 (2007)
31. Ahmed Z, et al. (HAPPEX) *Phys. Rev. Lett.* 108:102001 (2012)
32. Androić D, et al. (Qweak Collab.) *Phys. Rev. Lett.* 111:141803 (2013)
33. Arrington J, Sick I. *Phys. Rev. C* 76:035201 (2007)
34. Zhu SL, Puglia SJ, Holstein BR, Ramsey-Musolf MJ. *Phys. Rev. D* 62:033008 (2000)
35. Tanabashi M, et al. (Particle Data Group), *Phys. Rev. D* 98:030001 (2018) Section 10: "Electroweak Model and Constraints on New Physics"
36. Hall NL, Blunden PG, Melnitchouk W, Thomas AW, and Young RD. *Phys. Lett. B* 753:221 (2016)
37. Blunden PG, Melnitchouk W, Thomas AW. *Phys. Rev. Lett.* 107:081801 (2011)
38. Blunden PG, Melnitchouk W, Thomas AW. *Phys. Rev. Lett.* 109:262301 (2012)
39. Gorchtein M, Horowitz CJ, Ramsey-Musolf MJ. *Phys. Rev. C* 84:015502 (2011)
40. Gorchtein M, Spiesberger H, Zhang X. *Phys. Lett. B* 752:135 (2016)
41. Rislow BC, Carlson CE. *Phys. Rev. D* 83:113007 (2011)
42. Hall NL, Blunden PG, Melnitchouk W, Thomas AW, Young RD. *Phys. Rev. D* 88:013011 (2013)
43. Hall NL, Blunden PG, Melnitchouk W, Thomas AW, Young RD. *Phys. Lett. B* 753:221 (2016)

44. Gorchtein M, Horowitz CJ, Ramsey-Musolf MJ. *Phys. Rev. C* 84:015502 (2011)
45. Amherst: <https://www.physics.umass.edu/acfi/seminars-and-workshops/the-electroweak-box>
46. Green J, et al. *Phys. Rev. D* 92:031501 (2015)
47. Sufian RS, et al. *Phys. Rev. Lett.* 118:042001 (2017)
48. Young RD, Roche J, Carlini RD, Thomas AW. *Phys. Rev. Lett.* 97:102002 (2006)
49. Liu J, McKeown RD, Ramsey-Musolf MJ. *Phys. Rev. C* 76:025202 (2007)
50. Zhan, et al. *Phys. Lett. B* 705:59 (2011)
51. Antognini et al. *Science* 339:417 (2013)
52. Kelly JJ. *Phys. Rev. C* 70:068202 (2004)
53. Galster S, Klein, H, Moritz, J, Schmidt KH, Wegener D. *Nucl. Phys. B* 32:221 (1971)
54. Venkat S, Arrington J, Miller GA, Zhan X. *Phys. Rev. C* 83:015203 (2011)
55. Erler J, Ramsey-Musolf MJ. *Phys. Rev. D* 72:073003 (2005)
56. Erler J, Ferro-Hernández R, *J. High Energy Phys.* 1803:196 (2018)
57. Patrignani C, et al. (Particle Data Group), *Chin. Phys. C* 40:100001 (2016)
58. Ramsey-Musolf MJ. *Phys. Rev. C* 60:015501 (1999)
59. Wood CS, et al. *Science* 275:1759 (1997)
60. Dzuba VA, Berengut JC, Flambaum VV, Roberts B. *Phys. Rev. Lett.* 109:203003 (2012)
61. G. P. Zeller et al. (NuTeV) *Phys. Rev. Lett.* 88:091802 (2002)
62. Bentz W, Cloët IC, Londergan JT, Thomas, AW. *Phys. Lett. B* 693:462 (2010)
63. Langacker P. *Nucl. Phys. B Proceeding Supplement* 38:152 (1995)
64. D. Becker, et al. *Eur. Phys. J. A* 54:208 (2018)
65. Benesch J, et al. arXiv:1411.4088 [nucl-ex]
66. The Jefferson Lab PVDIS Collaboration. *Nature* 506:67 (2014)
67. Chen JP, et al. arXiv:1409:7741 [nucl-ex]
68. Zhao YX, et al. arXiv:1701:02780 [nucl-ex]
69. Young RD, Carlini RD, Thomas AW, Roche J. *Phys. Rev. Lett.* 99:122003 (2007)
70. Eichten E, Lane KD, Peskin ME. *Phys. Rev. Lett.* 50:811 (1983)
71. Erler J, Horowitz CJ, Mantry S, Souder PA. *Annu. Rev. Nucl. Part. Sci.* 64:269 (2014)
72. Bennett SC, Wieman CE. *Phys. Rev. Lett.* 82:2484 (1999)
73. Edwards NH, et al. *Phys. Rev. Lett.* 74:2654 (1995)
74. MacPherson MJD, et al. *Phys. Rev. Lett.* 67:2784 (1991)
75. Meekhof DM, et al. *Phys. Rev. Lett.* 71:3442 (1993)
76. Tanabashi M, et al. (Particle Data Group), *Phys. Rev. D* 98:030001 (2018) Section 112, "Searches for Quark and Lepton Compositeness", <http://pdg.lbl.gov/2018/reviews/rpp2018-rev-searches-quark-lep-compositeness.pdf>
77. Tanabashi M, et al. (Particle Data Group), *Phys. Rev. D* 98:030001 (2018) "PDGLive", <http://pdglive.lbl.gov/Particle.action?node=S054>
78. Tanabashi M, et al. (Particle Data Group), *Phys. Rev. D* 98:030001 (2018) Section 115, "Leptoquarks", <http://pdg.lbl.gov/2018/reviews/rpp2018-rev-leptoquark-quantum-numbers.pdf>
79. Tanabashi M, et al. (Particle Data Group) *Phys. Rev. D* 98:030001 (2018) "PDGLive", <http://pdglive.lbl.gov/Particle.action?node=S056>

**Table 1** Ingredients in the determination of  $Q_W^p$  from the  $Q_{\text{weak}}$  datum alone

Ingredient	Value (ppb)	Error (ppb)	Val/Tot (%)
$A_E$	-26.20	3.63	12%
$A_M$	79.88	1.36	35%
$A_E^s$	-1.11	0.33	0%
$A_M^s$	0.77	0.24	0%
$A_{ax}$	5.60	2.36	2%
$A_{had}$ total:	58.95	4.55	26%
$Q_{\text{weak}} A$	-226.50	9.30	100%
$A_{had} + Q_{\text{weak}}$	-167.55	10.35	74%
$A_0$	-2229.33		
$Q_W^p$	0.0752	0.0046	107%
$\gamma Z$ -box r.c.	0.0046	0.0005	7%
$Q_W^p - \gamma Z$	0.0706	0.0047	100%

**Table 2** Uncertainty contributions to  $A_{ep}$

Contribution	Uncertainty (ppb)
Statistical	7.3
Systematic:	
Rescattering bias: $A_{\text{bias}}$	3.4
BCM Normalization: $A_{\text{BCM}}$	2.6
Target windows: $A_{b1}$	1.9
Beamline Background: $A_{\text{BB}}$	1.4
Beam Asymmetries: $A_{\text{beam}}$	1.3
Kinematics: $R_{A^2}$	1.3
Beam Polarization: $P$	1.2
Total of 11 Others	2.3
Total Systematic	5.8
Total	9.3

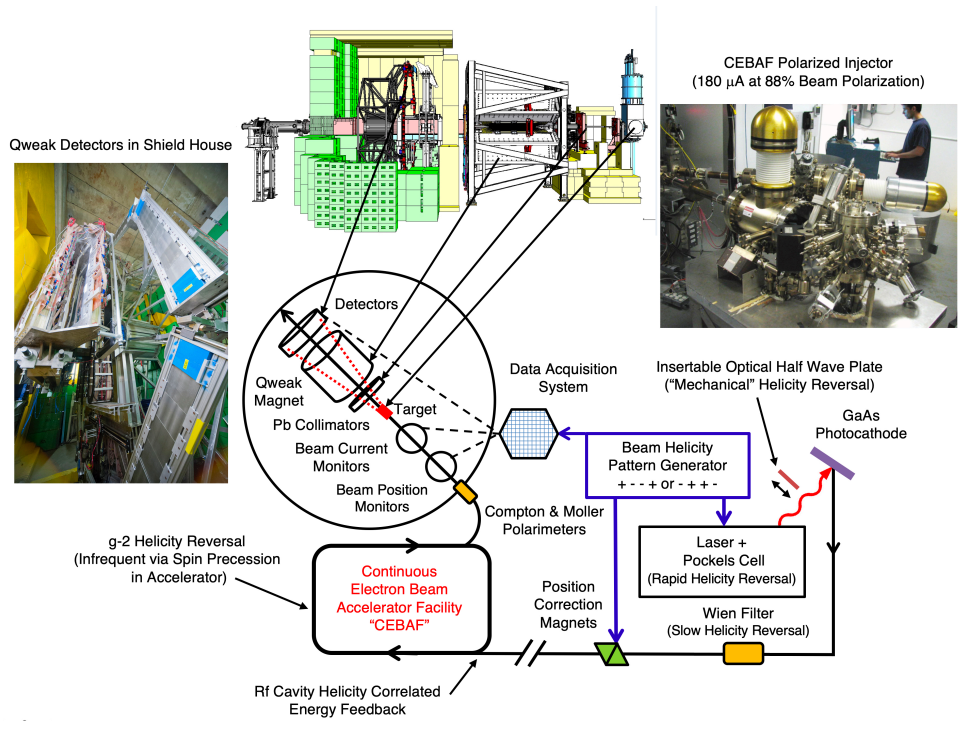


**Figure 1**

The key subsystems include: An ultra-stable superconducting accelerator (CEBAF) at Jefferson Laboratory, a GaAs polarized source for intense electron beams, a rapid pseudo-random spin reversal capability to permit the measurements to cleanly isolate the signature of the weak interaction, the periodic insertion of a half-wave optical plate into the laser drive of the GaAs source to reverse the electron beam helicity via a mechanical rather than electrical technique, periodic Wien filter and  $g - 2$  spin reversals during data taking to suppresses slow helicity correlated systematic effects, instrumentation to measure/control undesirable helicity-correlated changes in the electron beam parameters, a 0.34 m long liquid hydrogen target, a toroidal magnetic spectrometer to select elastically scattered electrons, an azimuthally symmetric Quartz Cerenkov detector system with custom built electronics employing ultra-low noise electronics and interchangeable PMT bases to permit use with traditional drift chambers during low luminosity calibration studies. Portions adapted from Reference (8).

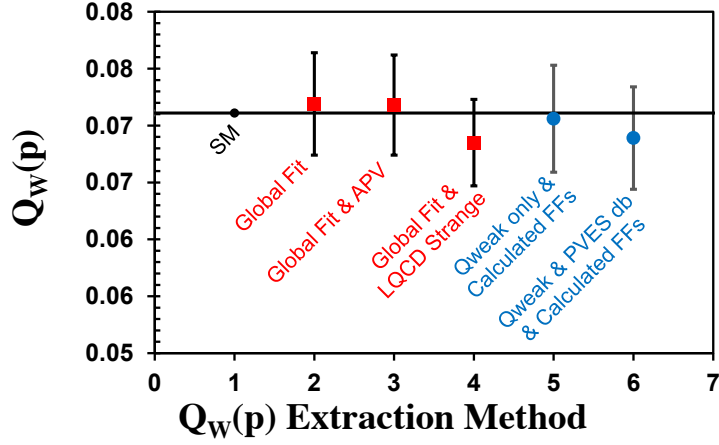


**Figure 2**

The values of the proton’s weak charge determined from each of the several methods discussed in Section 3 are compared with one another and with the SM prediction (“method 1” in the figure). The red points (see Section 3.1) show the result of a global fit incorporating the  $Q_{\text{weak}}$  datum together with the PVES database (method 2), the same including the APV result (method 3), or including LQCD calculations for the strange form factors  $G_{E,M}^s$  (method 4). The blue point (method 5) discussed in Section 3.2 uses just the  $Q_{\text{weak}}$  datum with calculated (instead of fit) axial and lattice strange form factors. The last point (method 6) discussed in Section 3.3 extends method 5 to include the  $\bar{e}p$  PVES database.

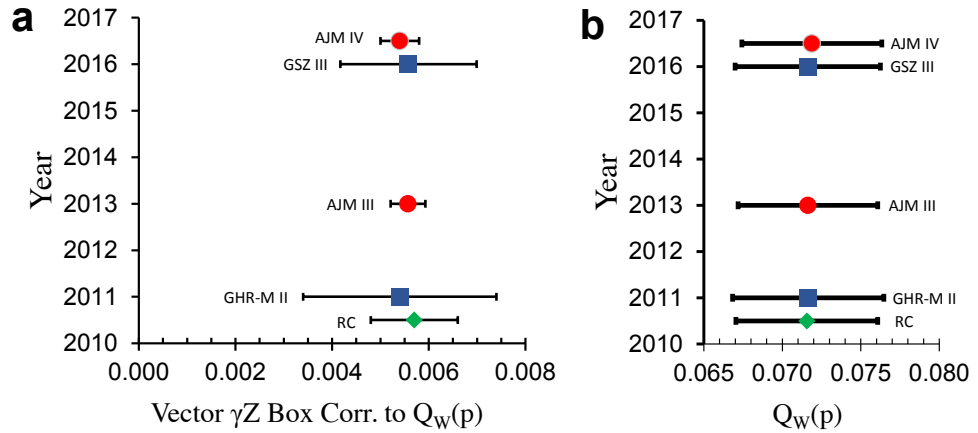


**Figure 3**

**a:** Calculations of the energy-dependence of the vector piece of the  $\gamma Z$ -box radiative correction from three groups since 2011. Blue squares: Gorchtein, et al. (39), green diamond: Rislow & Carlson (41), and red circles: the AJM (Adelaide-JLab-Manitoba) collaboration (42, 43). **b:** Determinations of the proton’s weak charge using the global fit method described in Section 3.1 for each of the calculated  $\square_{\gamma Z}^V$  radiative corrections in **a**.

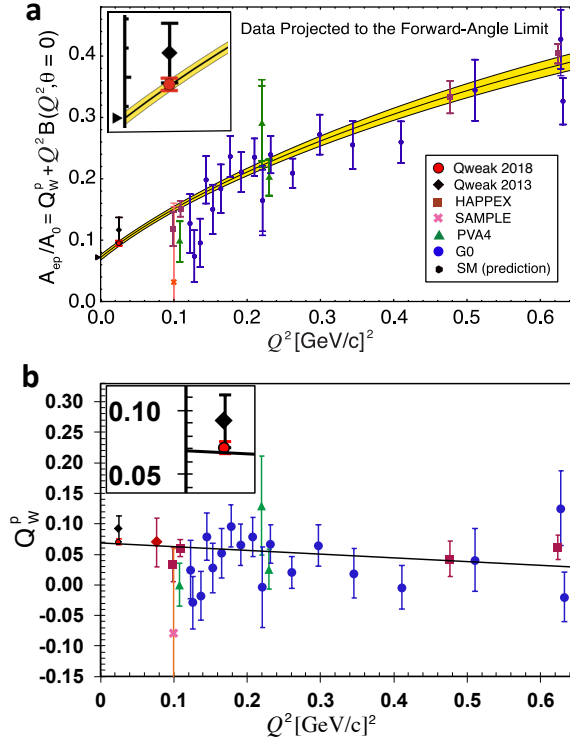


**Figure 4**

(a) Global fit (black curve) of the reduced asymmetries  $A/A_0$  constituting the PVES database, obtained by varying the weak vector quark couplings  $C_{1u}$  and  $C_{1d}$ , the strength of the strange form factors  $G_{E,M}^s$ , and the isovector axial form factor  $G_A^{Z(T=1)}$ . The yellow band indicates the uncertainty in the fit. The inset shows the region of the  $Q_{\text{weak}}$  experiment which dominates the fit. The legend indicates the different collaborations responsible for the data used in the fit, and also indicates the SM value of  $Q_W^p$  with the black arrowhead at  $Q^2 = 0$ . Adapted from Reference (8). In the lower figure (b), a linear fit (black line) is made to the  $Q_W^p$  obtained for each datum in the PVES database by calculating  $A_{EM}$ ,  $A_s$  and  $A_{ax}$  in Equation 11 for each measured asymmetry.

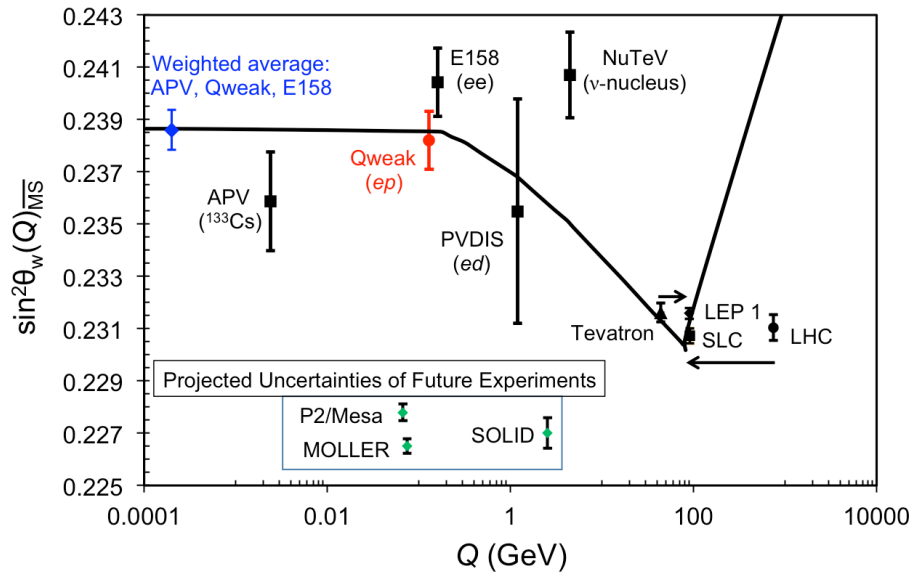


**Figure 5**

Variation of  $\sin^2 \theta_w$  with energy scale  $Q$ . The modified-minimal-subtraction  $\overline{MS}$  scheme prediction of the Standard Model is shown as the solid curve, along with existing experimental determinations and some proposed future measurements. References can be found in the text. The weighted average of the three low  $Q$  weak charge measurements is displayed at arbitrary  $Q$  to indicate the confirmation of the running of the weak mixing angle with  $9.6 \sigma$  significance. Adapted from Reference (8).

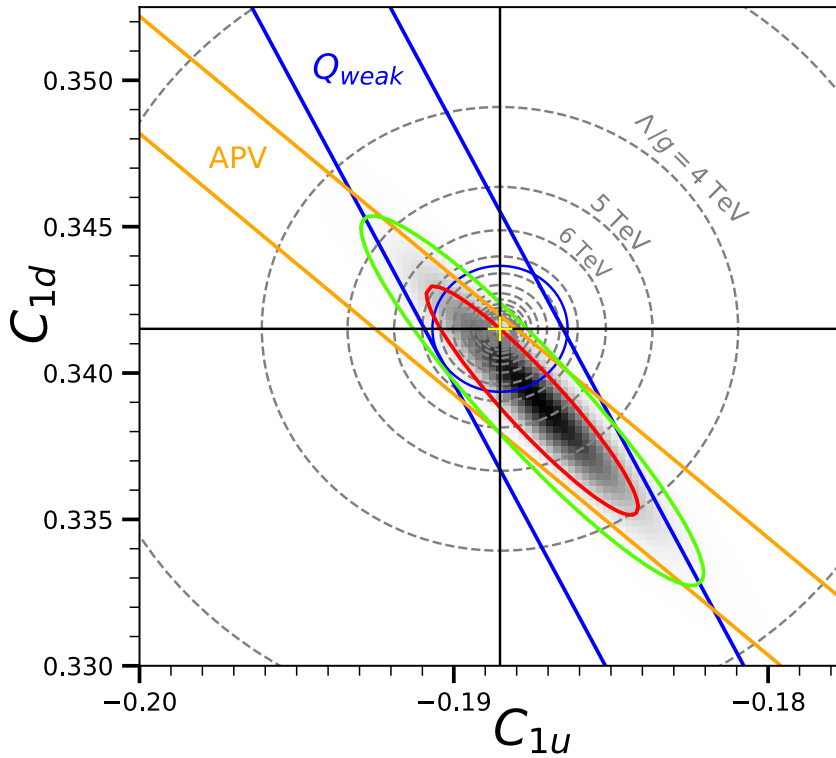


**Figure 6**

Contours of  $\Lambda/g$  in  $C1$  space. The SM origin is indicated by the yellow cross. The dashed circles are mass reach contours starting with  $\Lambda/g = 3$  TeV (outermost, incomplete contour) which increase in steps of 1 TeV at progressively smaller diameters. The 95% CL constraints provided by the Qweak and APV experiments are shown as the blue and orange bands, respectively. The 68% and 95% CL combined constraints from these two experiments are shown by the red and green ellipses, respectively. The solid blue circle indicates the 95% CL constraint provided by the Qweak experiment on the proton. Adapted from Reference (8).

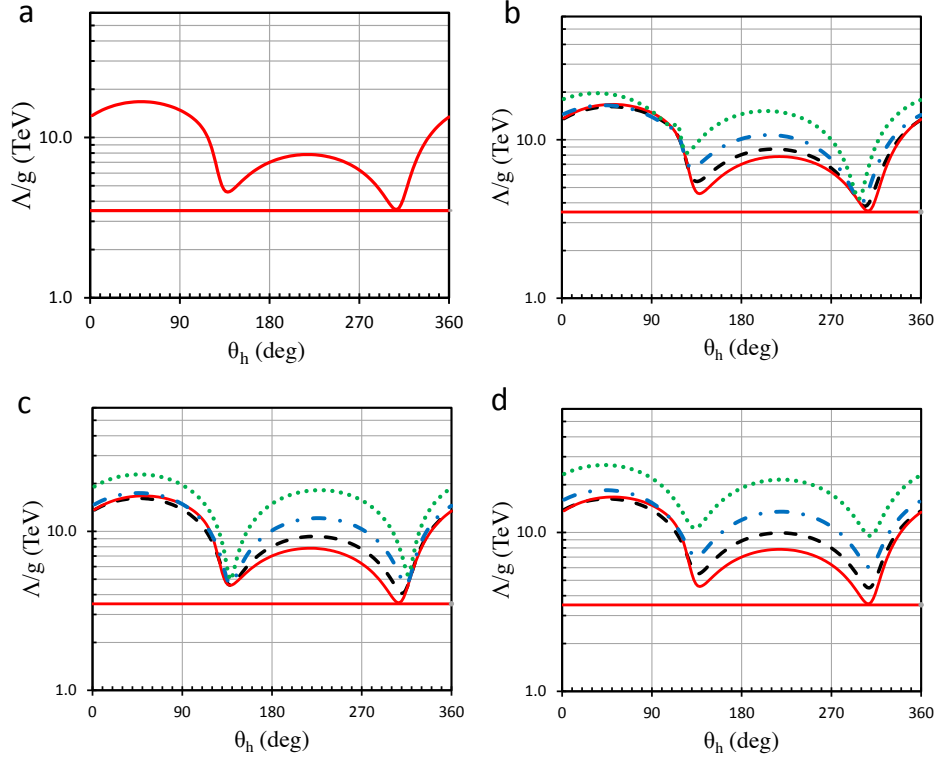


**Figure 7**

(a) A plot (solid red curve) of the mass reach  $\Lambda/g$  as a function of the flavor mixing angle  $\theta_h$  corresponding to the constraints provided by  $Q_{\text{weak}} \bar{e}p$  and Cesium APV experiments. The horizontal red line denotes 3.5 TeV. Adapted from Reference (8). (b) The three dashed curves denote what would happen with the addition of a future  $Q_W^p$  measurement with either  $\Delta Q_W^p = 0.0045, 0.0045/2, \text{ and } 0.0045/4$ . (c) The three dashed curves denote what would happen with the addition of a future APV measurement with either  $\Delta Q_W(\text{Cesium}) = 0.43, 0.43/2, \text{ and } 0.43/4$ . (d) The three dashed curves denote what would happen with the addition of future  $Q_W^p$  and APV measurements, each with uncertainties equal to those available in the existing measurements, half the existing measurements, and one quarter the existing measurements.

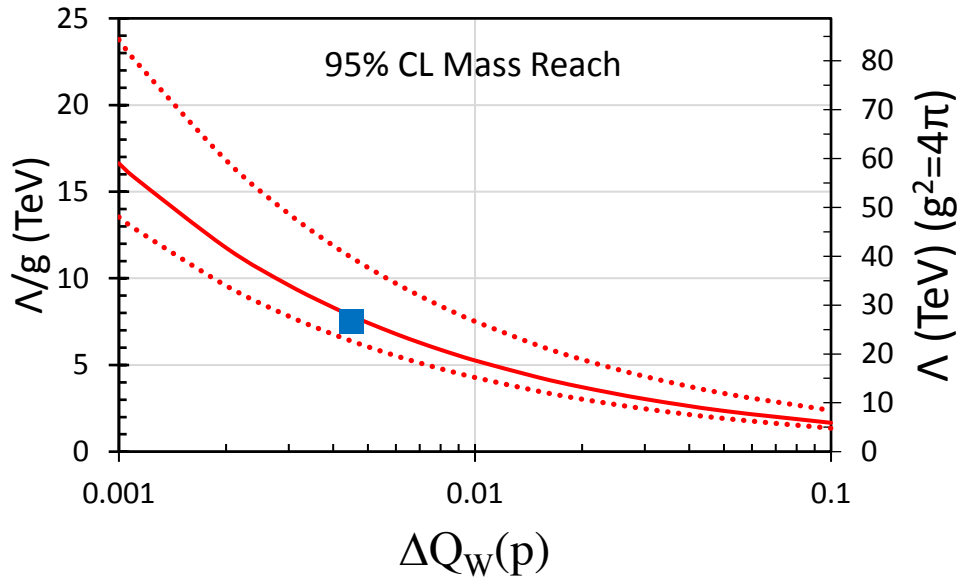


**Figure 8**

A plot of the 95% CL mass reach  $\Lambda/g$  (and  $\Lambda$  with  $g^2 = 4\pi$ ) as a function of the uncertainty  $\Delta Q_W^p$  in measurements of the proton's weak charge ( $\theta_h = 26.6^\circ$ ) assuming a central value  $Q_W^p$  on the SM. The blue square denotes the existing constraint provided by the  $Q_{\text{weak}}$  experiment's result (8) with an uncertainty of  $\pm 0.0045$  and a central value of 0.0719, which is  $+0.0008$  from the SM. The dashed lines denote the boundaries defined by  $\pm 1\sigma$  deviations of the assumed  $Q_W^p$  from the SM central value. Note that the uncertainty  $\Delta Q_W^p$  proposed for the P2 experiment (64) is about 0.0011, which has the potential to deliver about twice the mass reach achieved in the  $Q_{\text{weak}}$  experiment.